

PEARS Emission Line Galaxies

Nor Pirzkal¹, Barry Rothberg^{1,2,3}, Chun Ly^{1,4}, James E. Rhoads⁵, Sangeeta Malhotra⁵, Norman A. Grogin¹, Tomas Dahlen¹, Gerhardt R. Meurer⁶, Jeremy Walsh⁷, Nimish P. Hathi⁸, Seth Cohen⁵, Andrea Belini¹, Benne W. Holwerda⁹, Amber Straughn¹⁰, Matthew Mechtley⁵

ABSTRACT

We present a full analysis of the Probing Evolution And Reionization Spectroscopically (PEARS) slitless grism spectroscopic data obtained with the Advanced Camera for Surveys on *HST*. PEARS covers fields within both the Great Observatories Origins Deep Survey (GOODS) North and South fields, making it ideal as a random survey of galaxies, as well as the availability of a wide variety of ancillary observations to support the spectroscopic results. Using the PEARS data we are able to identify star forming galaxies within the redshift volume $0 < z < 1.5$. Star forming regions in the PEARS survey are pinpointed independently of the host galaxy. This method allows us to detect the presence of multiple emission line regions (ELRs) within a single galaxy. 1162 [OII], [OIII] and/or H α emission lines have been identified in the PEARS sample of ~ 906 galaxies down to a limiting flux of $\sim 10^{-18}$ erg/s/cm². The ELRs have also been compared to the properties of the host galaxy, including morphology, luminosity, and mass. From this analysis we find three key results: 1) The computed line luminosities

¹Space Telescope Science Institute, 3700 San Martin Drive, Baltimore, MD, 21210, USA

²George Mason University, Department of Physics & Astronomy, MS 3F3, 4400 University Drive, Fairfax, VA 22030, USA

³Leibniz-Institut für Astrophysik Potsdam (AIP), An der Sternwarte 16, 14482, Potsdam, Germany

⁴Giacconi Fellow

⁵School of Earth And Space Exploration, Arizona State University, Tempe, AZ, 85287-1404, USA

⁶International Centre for Radio Astronomy Research, The University of Western Australia, 35 Stirling Highway, Crawley, WA 6009, Australia

⁷European Southern Observatory, Karl-Schwarzschild-Strasse 2, D-85748 Garching, Germany

⁸Carnegie Observatories, 813 Santa Barbara Street, Pasadena, CA 91101, USA

⁹ESA Fellow, ESA-ESTEC, Keplerlaan 1, 2200 AG, Noordwijk, the Netherlands

¹⁰Astrophysics Science Division, Goddard Space Flight Center, Code 665, Greenbelt, MD 20771, USA

show evidence of a flattening in the luminosity function with increasing redshift; 2) The star forming systems show evidence of disturbed morphologies, with star formation occurring predominantly within one effective (half-light) radius. However, the morphologies show no correlation with host stellar mass; and 3) The number density of star forming galaxies with $M_* \geq 10^9 M_\odot$ decreases by an order of magnitude at $z \leq 0.5$ relative to the number at $0.5 < z < 0.9$ in support of the argument for galaxy downsizing.

Subject headings:

1. Introduction

Emission line galaxies (ELGs) are systems selected by the presence of strong line emissions (e.g. Ly- α [OII], [OIII], H β , and H α) usually detected from grism surveys. The emission lines in these galaxies trace recent star formation, in contrast to the history and properties of the stellar populations that can be discerned from only broad band observations. ELGs are an important population because they can be used to trace the star formation history of galaxies at various epochs owing to their ability to be easily detected via their strong emission lines (which also provides redshifts). Using ELGs allows one to probe down to lower luminosity (and thus lower mass) galaxies compared to broad band surveys which tend to be incomplete at or above m^* galaxies at more distant epochs. Assuming that ELGs are spatially distributed in a fashion similar to other galaxies, they provide a powerful tool for tracing the star formation history of the Universe.

The epoch $0 < z < 1.5$ is important because star formation activity in galaxies has been observed to increase significantly as redshift increases (Madau et al. 1998; Hopkins 2004, e.g.). At higher redshifts ($z > 2$) there is still some controversy remains as to whether the star formation density relation flattens or decreases but the initial increase in star formation implies that, at low z , some mechanism(s) must have occurred which quickly quenched it, else massive ellipticals today should still be forming many stars. Evidence suggests that the inter stellar medium, star formation rates and gas fractions differ between local and distant galaxies. This requires not only the ability to measure the star formation history, but to properly sample galaxies over a wide range of masses to alleviate biases. ELGs are ideal for such work. As noted above, they are easily detected in surveys and are more efficient for probing to lower stellar masses as a function of telescope time required. The wavelength range of the ACS grism used for PEARS makes it possible to identify the strong restframe emission lines [OII], [OIII], and H α out to $z \sim 1.5$. In this paper, examining H α , [OIII] and [OII] emitters allows us to look at properties of star forming galaxies in increasing redshift

ranges and when plotted separately they represent proxies for the redshift bins of $0 < z < 0.5$, $0.1 < z < 0.9$, and $0.5 < z < 1.5$, respectively.

Identifying ELGs has traditionally been done using narrow band photometric filters. This technique has been successfully applied to very high redshifts to detect Ly- α emitters. While narrow band surveys can efficiently cover large fields of view down to relatively faint magnitudes, they are typically limited to very small and discrete redshift ranges. This can be partially alleviated using multiple narrow band filters (Subaru Deep Field, Ly et al. 2007, e.g.). However, the properties of the host galaxies can also affect these surveys, particularly the ability to accurately estimate equivalent widths (EW). The Probing Evolution And Reionization Spectroscopically (PEARS) slitless grism spectroscopic survey provides an unprecedented opportunity to study ELGs in a way that cannot be achieved from any ground based observations. PEARS allows us to bypass the difficulties inherent in narrow band filter surveys (as noted above) and the limitations imposed by varying sky brightness and atmospheric emission lines which can limit ground-based grism surveys, and identify ELGs based *solely* on the direct detection of emission lines in dispersed slitless spectra. Based on previous experience, our selection is independent of the nature and brightness of the host galaxy and is sensitive to very high EW emission lines. Furthermore, the slitless data allows us to detect ELGs over a very large and continuous redshift range. As previously shown (Pirzkal et al. 2006; Straughn et al. 2008, 2009), this approach allows us to detect emission lines in very faint host galaxies, particularly sub- m^* galaxies. The unambiguous identification of star forming regions in ELGs (including multiple ELRs within a single galaxy) illustrates the strength of slitless spectroscopic observations. Moreover, since PEARS overlaps with both GOODS-N and GOODS-S, there exists a substantial amount ancillary data, including very deep imaging of the host galaxies. The redshift range ($0 < z < 1.5$) probed by PEARS is a critical transition epoch, both in terms of star formation histories and morphological evolution. Our robust data set makes it possible to examine these trends over a much wider mass range than has been previously probed.

This paper is organized as follow: Section 2 briefly summarizes the PEARS observations (HST Proposal 10530, P.I. Malhotra). Section 3 describes the data reduction and analysis of the sample, including detection, extraction and identification of emission lines, as well as completeness tests. Section 4.1 presents the PEARS [OII], [OIII] and H α line luminosity functions and their redshift evolution. Finally, Section 4.2 compares the properties of the PEARS host galaxies, such as morphology and luminosity, with the star formation properties discerned from the PEARS emission lines.

2. Observations

The PEARS observations were obtained as part of a large *Hubble Space Telescope* (*HST*) proposal (200 orbits, Proposal 10530; P.I.: Malhorta). The program used the Advanced Camera for Surveys (ACS) Wide Field Camera (WFC) in conjunction with the G800L grism filter. The G800L has a resolution of $R \sim 69\text{--}131$ and provides wavelength coverage of $0.55\text{--}1.05\ \mu\text{m}$ across the entire ACS/WFC field of view. A total of nine fields ($\approx 11.65\ \text{arcmin}^2$ for each field) were observed for $\approx 40000\ \text{s}$ (20 orbits) each, split evenly between observations taken at different position angles (P.A.) in the sky (typically 3 per pointing). Multiple P.A.s are important for identifying and masking contamination from other sources in the field and removing spurious pixels (e.g. cosmic rays, bad pixels, etc). Four PEARS fields are within the GOODS-N field (Giavalisco et al. 2004). Five PEARS fields are within the GOODS-S field, with one PEARS field re-observing the GRAPES/HUDF field (Pirzkal et al. 2004). The combined areas of the PEARS-N and PEARS-S are 50.24 and $68.84\ \text{arcmin}^2$, respectively. The fields and their location within the GOODS fields are shown in Figure 1. Table 1 lists the PEARS fields positions and total exposure times.

3. Data Reduction and Analysis

3.1. Detection of Emission Lines

Emission lines were detected directly from combined ACS grism slitless spectroscopic images. The basic method used to identify emission lines in the PEARS data was described previously in Straughn et al. (2008, 2009). However, only the PEARS-South data were used. Presented here are the full PEARS data set (comprising PEARS-North and PEARS-South). As such, we have employed a new, refined version of our line identification pipeline to search for the presence of emission lines down to a lower flux level than before. The new detection algorithm, dubbed “PEARS-2D,” is briefly summarized below:

- 1) All grism data obtained at the P.A. on the sky are combined using the PYRAF task `MULTIDRIZZLE` (Koekemoer 2002). This produces a high signal to noise image that is free of cosmic-ray and detector artifacts. This image was then smoothed using a 13×3 median.
- 2) The smoothed image was then subtracted from the Multidrizzle image. This removed the underlying continuum from the dispersed spectra. The continuum subtracted image was then used for the detection of emission lines.
- 3) The individual emission lines in each field were identified using SExtractor (Bertin & Arnouts 1996). This was repeated for each PEARS field and for each P.A. The output of each extraction was used to generate a list emission line candidates at each P.A. for each

field.

4) Using a detailed knowledge of the instrument distortions and of the dispersion relation of the G800L ACS/WFC grism, we were able to determine the location on the sky of individual emission lines across multiple P.A.s. This allowed us to construct accurate (to within one pixel) locations of the source of emission line and determine the observed wavelength of the emission line (See Figure 2 of Straughn et al. 2008). The detection threshold for the emission lines in the continuum subtracted images was set to 1.1σ . This threshold was selected because based on extensive previous experience with the ACS/WFC Grism it is highly unlikely that spurious flux will occur in the same location in the dispersed spectra at multiple P.A.s. Thus, the use of multiple P.A.s for slitless grism spectroscopy has been found to be quite effective at filtering out spurious detections. We further excluded any detections in which the ELR wavelengths were not consistent with each other to within 100\AA among the multiple P.A.s.

Using the PEARS-2D method we generated a list of ELR candidates for each PEARS field that did not rely at all on any pre-generated object catalogs or pre-selection of target galaxies. We stress that a candidate ELR did *not* require the detection of a host galaxy in the field. PEARS-2D, with its multiple P.A.s strategy, has three immediate advantages over other methods that rely on observations taken at a single P.A.: First, we can expect to detect extremely large EWs that would not be identified through more traditional techniques. Second, is the ability to derive accurate locations of the ELR without assuming that the source is at the center of the host galaxy. This has allowed us to identify multiple ELRs within a single galaxy. And, finally, it results in a wavelength calibration that is significantly more accurate. Normally, the wavelength reference point is tied to the location of the host galaxy (determined using a direct image taken in conjunction with the grism observations). However, since ELRs can be several half-light radii away (amounting to a non-trivial number of pixels) the wavelength solution of the ELR is affected by this distance from the center of the host galaxy. Every error of one pixel in the assumed position of the emission line feature results in a 40\AA systematic error in wavelength calibration. For large galaxies with multiple ELRs this can lead to errors on the order of several hundred \AA . With PEARS-2D, this error is avoided because the wavelength solution of the ELRs is determined *independent* of any information about the host galaxy.

3.2. Extraction and Verification of Spectra

The individual spectra of each of the ELRs identified in Section 3.1 were extracted using the regular PEARS pipeline (e.g. Pirzkal et al. 2009) with one exception. The pipeline requires a catalog of positions to use as the starting point for extracting spectra. Normally,

the catalog is generated from a direct image of the field in which the (presumed) sources of the spectra are identified and their positions measured (via Sextractor or some other method). For the work here, we generated a catalog based on the positions of the ELR candidates identified using the method described above. The extraction and calibration of the spectra were performed with aXe (Pirzkal et al. 2001; Kümmel et al. 2009) using optimally weighted extractions and an extraction width of $3\times$ the measured emission regions sizes. For each ELR candidate a separate spectrum was extracted for every P.A. observed. This resulted in 3 or 4 spectra extracted for each ELR candidate.

Rather than rely on automated schemes to accept or reject ELR candidates, the authors vetted each of the extracted spectra by eye. A catalog was generated which showed the multiple extracted spectra for each ELR candidate. The quality of the spectra and whether the spectra were foreground stars were assessed by each of the authors of the paper using a graded scale. Every spectrum extracted was graded a minimum of three times on a scale from 0 (very poor) to 5 (very high). An average grade was assigned to each and every ELR candidate. A final grade of 2 was found to correspond to a marginal ≈ 2 sigma detection of spectra obtained in at least two separate P.A.s. PEARS-2D generated 3705 ELR candidates. The quality assessment yielded a sample of 1162 emission lines (529 in PEARS-North and 633 in PEARS-South). We note here that in some cases multiple emission lines were detected in an ELR. The list of PEARS emission lines is shown in Table 2. The quality assessment produced a final number of 985 ELRs with an average grade of at least 2 (451 in PEARS-North and 535 in PEARS-South). As a final check, we compared our quality assessment to an automated method. We found that our grading methodology allowed us to reach a somewhat fainter line flux than could be achieved in an autonomous fashion. All of the analysis in this paper use [OII],[OIII], and $H\alpha$ emission lines with a final grade of 2.5 or above (177, 401, 174 emission lines, respectively)

3.3. Emission Line & Host Galaxy Identification

The resolution of the G800L grism is 40\AA pixel^{-1} is too low to resolve close emission line pairs (e.g. [OIII] and $H\beta$). However, at $0 < z < 1.5$, there are pairs of emission lines that fall within the wavelength range of the G800L grism and allow for both line identification (via the ratios of the two lines) and redshifts to be determined. The pairs detected in the sample were: [OII] and [OIII]; [OIII] and $H\alpha$; or CIII] and CIV.

However, in the majority of cases, we relied on a comparisons with photometric redshifts for the host galaxy from Dahlen et al. (2010, 2012). While the ELRs were selected independently, they were each subsequently matched with a host galaxy in the GOODS fields. The public ACS GOODS 2.0 data was used to generate mosaics of the GOODS fields. Sextractor

was then used to generate segmentation maps and object catalogs of galaxies. In the great majority of cases, the RA and DEC of a PEARS ELR clearly fell within the segmentation map of a galaxy. In such situations the corresponding galaxy was assumed to be the host of the ELR. Some ELRs were found to lie beyond any galaxy segmentation maps. However, restricting the selection criteria for detected lines to a PEARS grade of 2.5 or greater only $\approx 6\%$ of the PEARS ELR are located outside of the footprint of any GOODS galaxies. In these rare cases, we associated the ELR with the nearest segmentation map corresponding to a GOODS galaxy.

In the majority of cases, line identification and redshifts were made with single emission lines. At the onset, we assumed the line is from a specific subset based on the wavelength range of the observations (Ly- α , CIV, CIII], MgII, [OII], [NeIII], [OIII], H γ , or H α). Some of the emission lines discussed in this paper are blended lines, but this should have little effect on our analysis as weaker lines only weakly bias the fluxes and redshifts we derive. This is the case for [OIII] which is really two unresolved lines at 4959Å and 5007Å, H α at 6562Å which is blended with weaker [NII] at 6583Å, and the [NeIII] line refers to the stronger component at 3868Å.) For spectroscopic redshifts, 94% were in complete agreement with the 95% confidence regions of the photometric redshift catalogs. In which case the line identification is adopted. Where more than one ELR was identified in a given galaxy, the derived spectroscopic redshifts were found to be within $z = \pm 0.01$.

Some of the PEARS fields have multiple observations taken at different epochs. These observations were treated independently. This led to situations in which ELRs with multiple emission lines were detected several times (at different epochs). Nineteen such cases were identified (15 in PEARS-N and 4 in PEARS-S). In all cases the same lines were detected at the same observed wavelengths and with the same line fluxes. The line identifications and spectroscopic redshifts were also found to match within the errors. More quantitatively, the average difference in observed emission line wavelength, line flux, and redshift were: $\langle \delta\lambda \rangle = 18\text{Å}$; $\langle \frac{\delta f}{f} \rangle = 8\%$; and $\langle \delta z \rangle = 0.003$.

Finally, the line fluxes were corrected for Galactic Reddening assuming values from Cardelli et al. (1989). The corrections were $E(B-V)=0.012$ for PEARS-N fields and $E(B-V)=0.0078$ for PEARS-S fields.

3.4. Spectroscopic vs. Photometric Equivalent Widths for ELRs at Large Radii

One of the advantages of PEARS-2D is the ability to detect multiple ELRs within a single galaxy (see Figure 2). However, at progressively larger radii from the galaxy center the contribution from the underlying continuum decreases. Since spectra are extracted at

these large radii using small extraction windows, the measured EWs are generally larger than what would be derived by simply comparing the measured line fluxes to the total underlying continuum of the host galaxy. The EWs derived from narrow band imaging surveys generally rely on the latter method. To quantify any potential differences photometric EWs (EW_{phot}) were computed using the measured PEARS line flux and the measured total host galaxy broad band flux. On average the spectroscopic EW (EW_{spec}) was $\sim 3.5 \times (EW_{\text{phot}})$. Histograms of the EW_{spec} s for the [OII], [OIII], and $H\alpha$ are plotted in Figure 3. We note that for the purposes of this paper an emission line is reported as a positive EW.

3.5. Blended Emission Lines

The ACS G800L grism cannot separate the [OIII] doublet (4959Å, 5007Å) and $H\beta$ (4681Å). These three lines appear blended in the PEARS spectra. To correct for this, each of the lines were fit using separate components. We assumed identical full width at half maximum and assumed a fixed wavelength separation for all three lines. Based on this we obtained estimates of the [OIII] to $H\beta$ lines ratio for the ELRs. We found $\frac{f(H\beta)}{f([OIII])} \approx 0.23 \pm 0.25$, which is consistent with the relative fluxes expected in star forming galaxies (Juneau et al. 2011).

3.6. Completeness Simulations

In Table 4 the median and average line fluxes for [OII], [OIII], and $H\alpha$ with a strong detection (PEARS grade of at least 2.5) are listed. Figure 4 shows a histogram distribution of the line fluxes for the three lines. The histograms are plotted as a fraction of the total for each line. Figure 4 demonstrates that the PEARS-2D line fluxes peak at values of $\sim 10^{-17}$ erg/s/cm². The ACS G800L grism has an approximately flat sensitivity from $\approx 6000\text{Å}$ to 9500Å . As a result, our ability to recover emission lines from the two dimensional dispersed images needs to be carefully evaluated before we can say anything about the volume density of these sources. We determined the PEARS-2D detection limits using extensive end-to-end monte carlo simulations. These steps are briefly outlined here: First, we started with the real PEARS ACS/WFC data and artificially added a random distribution of simulated ELRs (and simulated emission lines) to the G800L images. A wide range of line fluxes, host galaxies, and redshifts were used. We also included random spatial distributions of ELRs, including locations on top or near a host galaxy. For the large host galaxies, up to 10 ELRs were added. Up to 100 lines were added each time. These simulations were repeated 10 times for *each* of the PEARS fields separately in order to account for the differences in

S/N and different spatial distribution of the host galaxies in each field.

Next, the simulated data were processed and identified using exactly the same procedures used for the real observations. The simulated spectra were extracted and line fluxes measured. For each PEARS field, the fraction of emission lines recovered as a function of line flux and observed wavelength was determined. The wavelength sensitivity was found to be very similar to the inverse sensitivity of the ACS G800L grism with sharp cutoff below 5500Å and above 10000Å. This set the redshift limits of the PEARS survey for the [OII], [OIII] and H α lines to be $0.5 < z < 1.6$, $0.1 < z < 0.9$, $0 < z < 0.5$, respectively. From this, we found the ability to successfully detect and accurately measure the flux of an emission lines was driven predominantly by the intrinsic flux in those lines. Therefore, ELRs with emission lines containing fluxes as low as 10^{-18} erg/s/cm² could be detected.

Finally, from this analysis we found that we could detect more than 50% of emission lines with flux greater than $\approx 3 \times 10^{-17}$ erg/s/cm². This is consistent with the observations shown in Figure 4. The exact fractions of lines recovered as a function of observed line flux for the PEARS-N, PEARS-S and PEARS-S-HUDF field (which is twice as deep as the PEARS-S fields) are shown in Figure 5.

3.7. Methods for Computing Luminosity Functions

3.7.1. The $1/V_{\max}$ method

This method does not assume a shape for the luminosity function $\Phi(L)$. However, one disadvantage is that it requires the data to be binned. The number of bins can impact the results. In this paper, the number of bins was determined using the Freedman-Diaconis rule (Freedman & Diaconis 1981), whereby the bin size is selected to be $2 \text{ IQR}(x)n^{-\frac{1}{3}}$, where IQR is the interquartile range of the data and n is the number of data points in the sample. Using the $1/V_{\max}$ method, the luminosity function is computed using the following formula:

$$\Phi(\log L_i) = \frac{1}{\Delta \log L} \sum_j \frac{1}{f(z_j, L_j) V_j} \quad (1)$$

where: $|\log L - \log L_i| < \frac{1}{2} \Delta \log L$; $\Delta \log L$ is the bin width; V_j is the maximum volume within which object j (observed to have a line flux of l_j and to be at the redshift of z_j) would be detected in our survey; and $f(z_j, L_j)$ is the incompleteness $f(l)$. The last parameter, $f(l)$, is a function of observed line flux (see 3.6) remapped into absolute luminosity space L given the object's redshift z_j , and is defined as:

$$V_j = \frac{\Omega}{4\pi} \int_{z_{j,\min}}^{z_{j,\max}} \frac{dV_c(z)}{dz} dz \quad (2)$$

where: Ω is the solid angle of our survey (sr); $V_c(z)$ is the cosmological comoving volume at redshift z (in Mpc^3); Given the redshift range $\{z_1, z_h\}$ at which a given emission line can be observed by the ACS grism (i.e. observed at wavelengths $6000\text{\AA} < \lambda < 9000\text{\AA}$), the minimum redshift, $z_{j,\min}$ is z_1 while the maximum redshift $z_{j,\max} = \min(z_h, z_{\text{faint}})$, where z_{faint} is the maximum redshift at which a line with luminosity L would remain above our minimum line detection threshold $l_{\text{threshold}}$. Hence, z_{faint} is the redshift corresponding to the distance of $D_L(z_j)\sqrt{l_j/l_{\text{threshold}}}$, where $D_L(z_j)$ is the luminosity distance of object j .

3.7.2. STY method

The STY method was also used for estimating the luminosity function. In this one, one assumes that $\Phi(L)$ has the form of a Schechter function (Schechter 1976):

$$\Phi(L)dL = \Phi_* \left(\frac{L}{L_*}\right)^\alpha \exp\left(-\frac{L}{L_*}\right) \frac{dL}{L_*} \quad (3)$$

which is characterized by the three parameters α , Φ_* , and L_* . Following from Sandage et al. (1979), the probability of observing a given object j at redshift z with a luminosity L_j , is then:

$$p(L_j, z_j) = \frac{\Phi(L)f(z_j, L_j)}{\int_{L_{\text{faint}}}^{\infty} \Phi(L)f(z_j, L)dL} \quad (4)$$

The joint likelihood can then be computed for the whole group of observed lines:

$$L = \prod_j p(L_j, z_j) \quad (5)$$

From this, can then determine values of α and L_* that maximizes this likelihood. The overall normalization constant Φ_* cannot be determined this way, because it cancels out in Equation 4. In this paper, we determined the values of α and L_* by maximizing Equation 5 using a Monte Carlo Markov Chain approach. This allowed us to determine the most likely values of these two parameters as well as 95% credible intervals for these parameters. Φ_* was computed by integrating Equation 3 and normalizing the result so that matched the number of detected objects. Φ_* was computed for each combination of α and L_* in our Markov Chains to produce 95% credible intervals for the parameter Φ_* .

3.7.3. Host galaxy SED fitting

Properties of the host galaxies of the PEARS ELRs were estimated by fitting model Spectral Energy Distributions (SEDs) to their broadband photometric colors. The photometric values were taken from the TFIT GOODS measurements, which include 10 and 12 photometric bands in the GOODS-N and GOODS-S, respectively (Laidler et al. 2007; Grogin et al. 2012). The photometry spans the observed UV (U -band) through thermal-IR based on VLT, *HST* and *Spitzer* observations. The actual SED fitting was done using our own Monte Carlo Markov Chain SED fitting code (π MC²) (Pirzkal et al. 2012) to obtain estimates of the stellar masses, extinction, and ages of the host galaxies. π MC² is a far more robust method of SED fitting than the standard χ^2 algorithms because it takes into account a proper treatment of both error propagation and computation of confidence levels. A more detailed explanation of MCMC can be found in (Pirzkal et al. 2012) and references within.

A simple stellar population model from BC03 (Bruzual and Charlot 2003) templates and a Salpeter IMF were used. While the choice of IMF and input models (e.g. BC03 or Maraston (Maraston 2005)) can affect derived stellar masses, the effects are not the same at all redshifts. The detailed simulations presented in Pirzkal et al. (2012) show that for the redshift range of interest here, stellar mass estimates from different models are consistent with each other to within a factor of a few. Other parameters obtained from SED fitting (e.g. extinction, metallicity and ages of the stellar population) are significantly more uncertain. For the purposes of this paper, we are primarily concerned with stellar mass, and to some extent extinction. In Figure 6 we show the distribution of stellar masses and extinctions for the host galaxies of the PEARS emission line sample. The mean stellar masses of the host ELGs are $\text{Log}(\text{mass}) = 8.74 \pm 0.97 \text{ M}_{\odot}$. We also estimate that the continuum extinction is relatively low with an average value of $A_v = 0.87 \pm 0.88 \text{ mag}$.

3.8. Internal Dust corrections to Luminosity Functions

Using the current PEARS data, there was no way to directly infer the amount of internal (to the host galaxy) dust attenuation affecting the line luminosities. We tested three methods for approximating dust corrections and compared the dust correction luminosity functions to the ones from Ly et al. (2007). The first dust correction used attenuation values from the individual SED fits to the host galaxies.

The second method we used to correct for dust extinction relied on applying an average extinction value of $A_{H\alpha} = 1.0 \text{ mag}$ (corresponding to $A_{[\text{OII}]} = 1.88 \text{ mag}$ and $A_{[\text{OIII}]} = 1.36 \text{ mag}$), as is commonly done in such a case (Hopkins 2004; Takahashi et al. 2007). While these two first approaches are straight forward, they are a rather crude attempt at

applying dust correction. Indeed, these approaches do not allow for the extinction values within ELRs to be different than the host galaxy as a whole and therefore does not account for the fact that ELRs are likely to contain more dust than the host galaxy as a whole.

The third method relied on a dust correction based on the somewhat more sophisticated luminosity dependent dust correction of Hopkins et al. (2001) and empirically attempts to circumvent this limitation. In this case, the amount of dust correction is related to the measured line luminosities and could hence have an effect on the shape of the luminosity functions we derive.

We find however that the three methods of correcting for dust had only limited influence on the luminosity functions. Either simply shifting the luminosity functions by a fixed amount without affecting the slope (α) at all (as is the case when using the first two methods), or altering the slope (α) only slightly (as is the case when applying a luminosity dependent dust correction). As expected, the [OII] lines were more affected by dust than the [OIII] and H α lines. However, in totum, for [OII], [OIII], and H α the slopes varied by ~ 0.1 on average either method. This is the same or smaller than the errors in Table 5.

4. Results

4.1. The Emission Line Regions

4.1.1. Star Forming Galaxy Density

Using the uncorrected PEARS lines listed in Table 4, we can begin by computing a space density of star forming galaxy (SFG), as measured by the PEARS survey, and compare it to previous ACS grism based surveys. We estimate the star forming galaxy density at $0.3 < z < 1.3$ to be $4.5 \times 10^{-3} \text{ Mpc}^{-3}$. This is in complete agreement with previous pure parallel ACS grism surveys such as the one described in Drozdovsky et al. (2005).

4.1.2. Luminosity Functions

We computed the luminosity functions for the [OII], [OIII], and H α samples using both the $1/V_{\text{max}}$ method and the STY methods that we described in Sections 3.7.1 and 3.7.2. The non dust-corrected luminosity functions, computed using the $1/V_{\text{max}}$ method are shown in Figures 7 to 9. In these figures, the new measurements are compared to those of (Ly et al. 2007, shown with open triangles and also uncorrected for dust). We added one additional constraint to the data from Ly et al. (2007). The comparisons were made only with objects

from that paper with an EWs $> 50\text{\AA}$.

The results from PEARS agree fairly well with earlier results, although they probe lower line luminosities for [OIII] and $H\alpha$. The results from PEARS-North and PEARS-South are plotted separately in Figures 7 to 9. The differences between these two large and independent fields are well within the errors. Table 5 summarizes the results from fitting the luminosity functions to each of the emission lines in each field separately and PEARS-North and -South together for both the $1/V_{\text{max}}$ and STY methods. Table 5 also includes the associated 95% credible intervals.

Figures 7 to 9 plot the results based on the $1/V_{\text{max}}$ method. When using the $1/V_{\text{max}}$ method, as previously noted in Section 3.7.1, the choose of bin size is important. We illustrate the effect of various bin sizes by showing (using light shaded circles) the luminosity functions we compute while allowing the bin sizes to vary. As one can visually witness, the effect of bin size has an immediate effect on the values with derive at a given luminosity. We show the luminosity derived using the optimal bin sizes using solid symbols. Error bars associated with individual points were derived using a few thousands bootstrapping iterations.

Here, we briefly note that the STY method produces steeper slopes than $1/V_{\text{max}}$ for [OII]. Yet for [OIII] and $H\alpha$ the two methods are consistent with each other. The differences between the two are likely due to the limited number of sources over a wide redshift range. This underlines the difficulties in obtaining luminosity function estimates with limited numbers of sources as well as the impact of different methods for deriving those estimates. We further note that the results shown in Figures 7 to 9 are also generally consistent with those from Ly et al. (2007). The differences are likely from the different limits in sensitivity to lower line fluxes between the two samples.

4.1.3. Do Luminosity Functions Evolve with Redshift?

Two advantages of the PEARS-2D sample are: that it reaches to faint line fluxes (a few times $10^{-18}\text{erg/s/cm}^2$); and the wide redshift range coverage. These can be used to investigate whether or not the slope of the luminosity functions changes with redshift. A change in the slope of the luminosity function as a function of redshift is a strong indication of evolution of how star formation has being occurring in the past ≈ 9 billions years. To examine this issue, each of the emission lines was divided by redshift, first into two bins, then into three bins. A luminosity function was fit to the data in each redshift bin (see Table 5). This allowed us to compute slopes for different redshift ranges. These slope are plotted against redshift in Figure 10. The “resolution” (number of bins) in 10 is limited by the available number of sources. Figure 10, shows a significant decrease in the value of α

as redshift increases for [OII], [OIII], and $H\alpha$ at both “resolutions.” This is consistent with earlier results from Ly et al. (2007). It suggests an evolution in ELGs and their capability to form stars over the last several Gyr as the proportion of high to low SFR regions increases as redshift increases.

4.1.4. *The Spatial Distribution of ELRs*

A major difference between PEARS-2D and other ELG studies is that we are able to detect the presence of multiple ELRs within a single galaxy. A breakdown of the sample shows that 69% of the ELGs contain a single ELR; 24% contain two ELRs; 4% contain three ELRs; and 3% contain four or five ELRs.

4.1.5. *Star Formation Rates of ELGs*

One of the most important question in galaxy evolution is whether the SFR changes over time, and if so, what shape does SFR vs redshift have. Assuming that ELGs are representative of star forming galaxies in general, the depth of the PEARS-2D study and the large redshift range allows us to tackle this important question. The SFR was calculated for the [OII] and $H\alpha$ emission lines using the Kennicutt (1998) relations. For [OIII] which are likely to actually be blended [OIII] and $H\beta$ the relation from Equation 5 in Drozdovsky et al. (2005) was adopted. The results are shown, as a function of redshift in Figure 12. Also plotted (using a black solid line) is the SFR for emission lines with an observed flux of $3 \times 10^{-17} \text{ erg/s/cm}^2$. This corresponds to the PEARS-2D 80% completeness level (solid black solid line). This illustrates our ability to detect emission line uniformly from $0 < z < 1.5$.

Simply computing the SFR does not provide an entirely accurate assessment of star formation because the mass of the galaxy affects the rate at which stars form. Instead, one can normalize the SFR by the mass of the galaxy (in this case estimated from the stellar masses computed in Section 3.7.3) to derive the specific SFR (sSFR). A histogram of the sSFR for the PEARS-2D ELGs is shown in Figure 13.

As the sSFR value of a galaxy can be taken, as a rough approximation, as one over the built up time of a galaxy, assuming constant star formation rate, the PEARS ELGs sSFRs implies a possible stellar mass built-up time of a few billions years. Note however that these sSFR estimates should be considered to be lower limits since some non detected star formation might be present in the PEARS ELGs and the SFR values we quote are not corrected for extinction.

There has been some discussion (Guo et al. 2011) as to whether the SFR in star forming regions of galaxies should be correlated to the location of the star forming regions within the galaxy. We investigate this possible relation using the PEARS ELG sample. Figure 14 shows a plot of the estimated SFR of each ELR in the PEARS-2D sample, separating [OII], [OIII] and $H\alpha$ emitting regions, as a function of radial distance of the ELR (normalized to the half light radius of the galaxy). As this Figure shows, we see no indication for trend as a function of ELR location for either of the three types of ELGs we examine. A simple Pearsons linear correlation test for [OII], [OIII] and $H\alpha$ yields values of -0.05, -0.001 and 0.04, respectively, indicating no statistical correlation between location of ELRs and SFR in those ELRs.

Finally, Figure 15 compares Log SFR against Log M_* for the ELGs in the PEARS-2D sample (open circles in all panels). The ELGs are plotted in four redshift bins to match the work of Noeske et al. (2007). In that work Noeske et al. (2007) derived a “main-sequence” of star forming galaxies for field galaxies in the Extended Groth Strip, complete to Log $M \sim 10.8$ (Figure 1 in that paper). The red squares shown in Figure 15 are the median values for the galaxies in Noeske et al. (2007) along with the $\pm 1\sigma$ (dotted red line). The conclusion was that there exists a gradual decline in SF of most galaxies since $z \sim 1$. The implication is that the same physics that regulates SF in local disk galaxies is occurring, which could be either an evolution in the gas supply or changes in the SF efficiencies. Noeske et al. (2007) suggested that the slope of the “main-sequence” is related to the gas exhaustion of galaxies and is related to the age of the galaxy and SF timescale, all of which are dependent on the galaxy mass. The PEARS-2D sample probes galaxies to much lower masses than those in Noeske et al. (2007). As such, we compare our galaxies to those in Noeske et al. (2007) in Figure 15. From this we can conclude that the relation we observe between SFR and host galaxy stellar mass is consistent with the star formation “main sequence” of objects with stellar masses of $\approx 10^{10} M_\odot$, while extending this relation by about four orders of magnitudes in mass. We also potentially witness a flattening of the sSFR versus mass relation for lower mass objects (below $\approx 10^8 M_\odot$). The dashed horizontal lines in Figure 15 show our sensitivity limits at the lower and higher ends of the redshift ranges we show and it is clear that the flattening of this relation is not caused by incompleteness, especially at the higher redshifts.

4.2. The Host Galaxies

4.2.1. Morphologies

The PEARS-2D galaxies comprise a remarkably robust sample to test the evolution of ELGs and compare their morphologies with properties such as SFRs and stellar masses. Unlike many morphological studies, our sample was not pre-selected by redshift or luminosities. This sample serves as a random selection of star-forming galaxies within the PEARS redshift volume, which is mostly unbiased by the actual morphology of these star-forming galaxies. In this section, we parameterize the morphologies of the host galaxies using the Gini Coefficient G and M_{20} parameters (Lotz 2004). The G and M_{20} parameters can be thought of as proxies for clumpiness and concentration coefficients and have been shown to be a good way to distinguish between “normal” galaxies and galaxy mergers in the local Universe, as demonstrated by Lotz (2004) in the blue using Sloan g -band, B_J , Thuan-Gunn g , and B -band (all corresponding to $\approx 4300 - 4500\text{\AA}$), as well as at $\sim R$ -band. Local spiral and elliptical galaxies follow a well defined sequence (e.g. Figure 9 in Lotz (2004)), while mergers have larger G and smaller M_{20} values (Lotz 2004, 2008, 2010). In order to compare the PEARS ELGs to galaxies in general, we computed the rest-frame G and M_{20} coefficients for both the PEARS ELGs as well as the entire GOODS catalog using the GOODS 2.0 ACS public data. These values were measured in all available observed wavelengths and a $\lambda \sim B$ -band (or $\sim 4350\text{\AA}$) rest-frame value was obtained by linearly interpolating between these measurements. When the rest-frame 4350\AA was outside of the available bands, the closest band was adopted.

As a comparison, we have also included field galaxies from within the same GOODS fields using the GOODS 2.0 ACS public data. For these objects, photometric redshifts were used to derive rest frame B band values for G and M_{20} . The rest-frame values of G and M_{20} were computed using linear interpolation of the values measured in each of the available bands, and the closest band was used when interpolation was not possible. The galaxies are all plotted in Figure 16, which is divided into three panels for clarity. The field galaxies from GOODS are plotted as contours, and in each panel the [OII], [OIII], and $H\alpha$ ELGs are shown separately. The solid line in Figure 16 delineates disturbed galaxies (above the line) from “normal” galaxies (below the line) according to Lotz (2004). When compared to the rest of the GOODS galaxies (black contours), the PEARS ELGs clearly have higher G and M_{20} values and fall above the fiducial line separating quiescent galaxies and active galaxies (from Lotz 2004). This strongly suggests that the PEARS ELGs have perturbed morphologies, likely due galaxy interactions.

Figure 16 implies that the PEARS-2D ELGs have disturbed morphologies, likely from some type of interaction. However, there is no correlation between the Gini- M_{20} values

and computed SFRs and stellar masses. To test for any correlation correlation, the Pearson Correlation coefficient (r) was used. It tests the degree of linear correlation between two independent data sets. r ranges in value from -1 to +1 (perfect negative or anti-correlation to perfect positive correlation). The most correlated relation we find is that of the [OIII] versus stellar mass, shown in Figure 17, which is very weak with a value of $r = 0.16$. All other relations show no statistical correlations.

4.2.2. 4350Å Rest-frame Luminosity of ELGs

The underlying host galaxy luminosity may provide additional information about the nature of the ELGs and how they compare to other galaxies in the field. Absolute magnitudes at 4350Å ($M_{4350\text{\AA}}$) were computed for both the ELGs and GOODS field galaxies. Figure 18 shows a histogram distribution of $M_{4350\text{\AA}}$ for the ELGs, divided into three panels, one for emission line. The median $M_{4350\text{\AA}}$ s as a function of the emission line are: -21.2 for [OII]; -19.0 for [OIII]; and -18.2 for H α .

One important question is whether the ELGs are representative of other galaxies within the same volume. As discussed in the Introduction, ELGs are incredibly useful for probing the evolution of the SFR not only out to more distant epochs, but down to fainter luminosities (and thus lower masses) than other galaxies. Figure 19 compares the luminosity function of the ELGs (separated by emission line which, again, we point out approximates different redshift bins) compared with field galaxies from GOODS, also delineated by redshift. Figure 19 clearly shows that the maximum density of [OII], [OIII], and H α occurs at much brighter levels than the depth of the GOODS data. While the luminosity functions of the GOODS field galaxies increases monotonically in a Schechter-like manner, the number of low mass line emitters decreases quickly. It is unlikely this trend is due to incompleteness. The PEARS-2D method is more sensitive to higher equivalent width lines, therefore we would expect to see *more* emission lines with observed flux levels of 3×10^{-17} erg/s/cm² when the continuum light from host galaxies decreases. Yet, there appears to be an absence of faint emission line galaxies in all three sub-samples.

To further quantify the effect, we examined the volume densities of [OIII] emitting galaxies at redshifts from 0 to 0.9. This is the redshift range with the largest number of ELGs. We imposed a further restriction and only selected galaxies above the completeness limit. This group was then divided into two subsets ($0 < z < 0.5$ and $0.5 < z < 0.9$) to see if the trend remained. The results are plotted in Figure 20 for $M_{4350\text{\AA}}$ (*left*) and Log Stellar Mass (*right*). The left panel of Figure 20 confirms that there appears to be a relatively small number of faint galaxies with detected [OIII] emission at higher redshifts. Recall that these host galaxies were selected solely based on the direct and independent detection of [OIII] in emission and

thus independently of their observed size and host luminosity. Our completeness simulations show the sample is sensitive to lines with flux $> 3 \times 10^{-17}$ erg/s/cm² and EW $> 50\text{\AA}$.

In the right panel of Figure 20 the stellar masses are compared for the two redshift ranges (same limits on sample selection as the left panel). The stellar mass distribution of galaxies with detected [OIII] emission differs significantly. At lower redshift there appears to be fewer massive galaxies with detected star formation. We conclude that, strongly star forming galaxies were on average more massive at higher redshifts. These results seem consistent with downsizing (Cowie et al. 1996, e.g.).

5. Conclusion

We have presented a sample of ELGs selected independently by their emission lines without *a priori* knowledge of their host properties. The methodology used (PEARS-2D) is based on *direct* detection of emissions line from *HST* slitless grism spectroscopy, with the added bonus of being able to detect multiple ELRs within a single galaxy. This has allowed us to construct a sample which is effectively random, and blind to other parameters. Using the wealth of ancillary data, we then investigated and compared the properties of the underlying hosts with the SFR histories derived from the ELRs. The key results are summarized below:

- 1) There is evidence for evolution in the luminosity function of [OII],[OIII] and H α emission lines. The slopes increase as a function of redshift.
- 2) The morphology of the host galaxies clearly indicates that these objects are disturbed, although we detect no correlation between morphology and our stellar mass estimates, star formation intensity, or the number of emission line regions in the host galaxies.
- 3) The mass density function of [OIII] emitting galaxies at $0 < z < 0.9$ strongly decreases. The number density of objects with stellar masses greater than $\approx 10^{10} M_{\odot}$ undergoing strong SF decreases at lower redshifts. This supports the idea of downsizing (Cowie et al. 1996, e.g.).

The results presented here also demonstrate the clear advantage of space-based grism spectroscopy. Such observations are able to probe deeper than similar ground-based studies. The PEARS-2D method also provides a method for detecting multiple ELRs allows spatial information about SF to be derived for galaxies. Future work will include using the WFC3 grism mode, with observed wavelength coverage of 0.8-1.6 μm . This will allow us to probe to significantly higher redshifts and determine whether the trends reported here continue to earlier epochs.

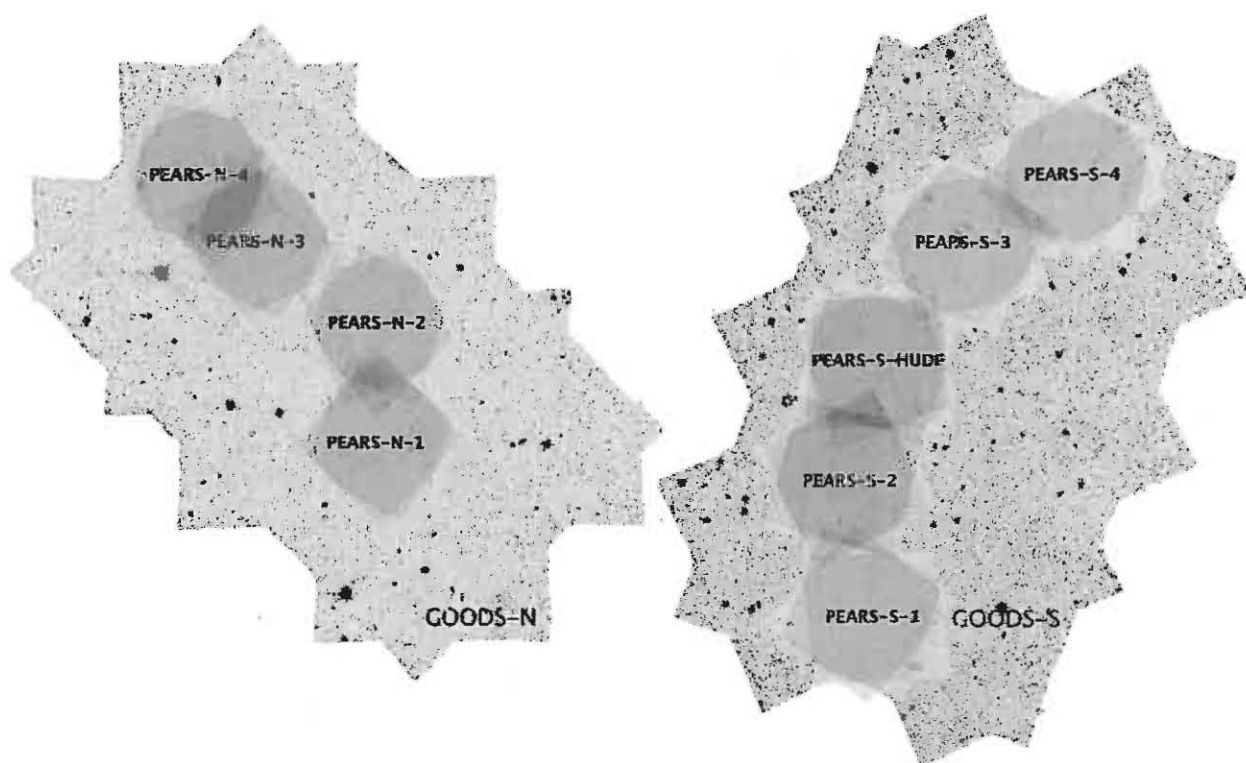


Fig. 1.— The location of the four PEARs-N (left) and five PEARs-S fields (right) within the GOODS-N and GOODS-S fields. The fields are oriented so that North is pointing up. Each of the shown PEARs field approximately is $200''$ arc second wide. Note that the total area where PEARs fields overlap is higher in PEARs-N than in PEARs-S.

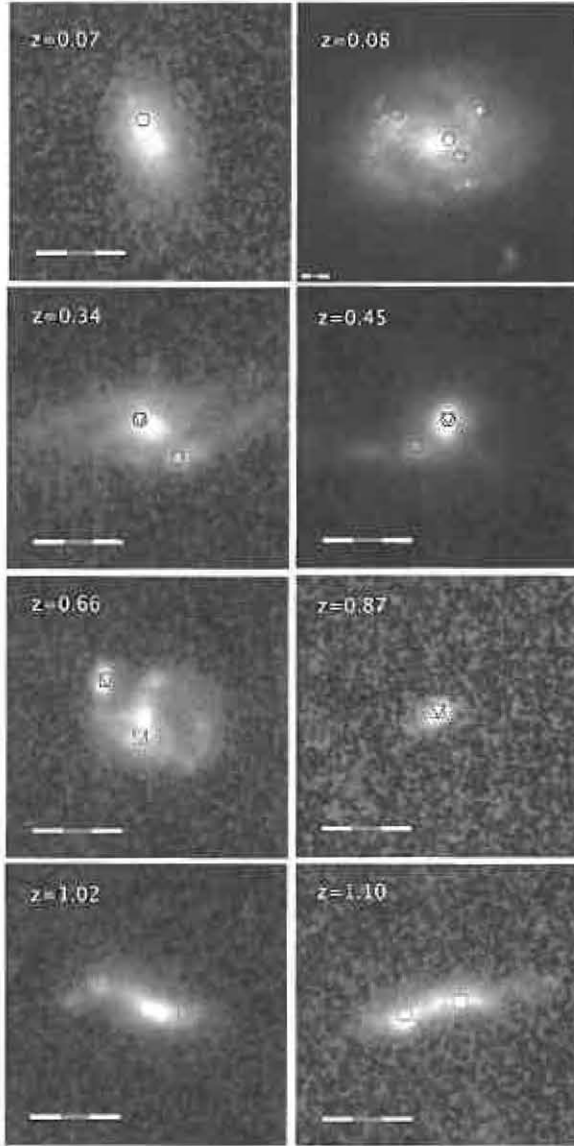


Fig. 2.— A sample of PEARS star forming galaxies with their identified star forming regions where emission in OII (red squares), [OIII] (green triangles) and H α (blue circles) are marked. The redshift is indicated at the top left of each stamp image and the a one arc second scale is shown at the bottom left of each stamp images. Multiple symbols are shown for regions where multiple lines were detected.

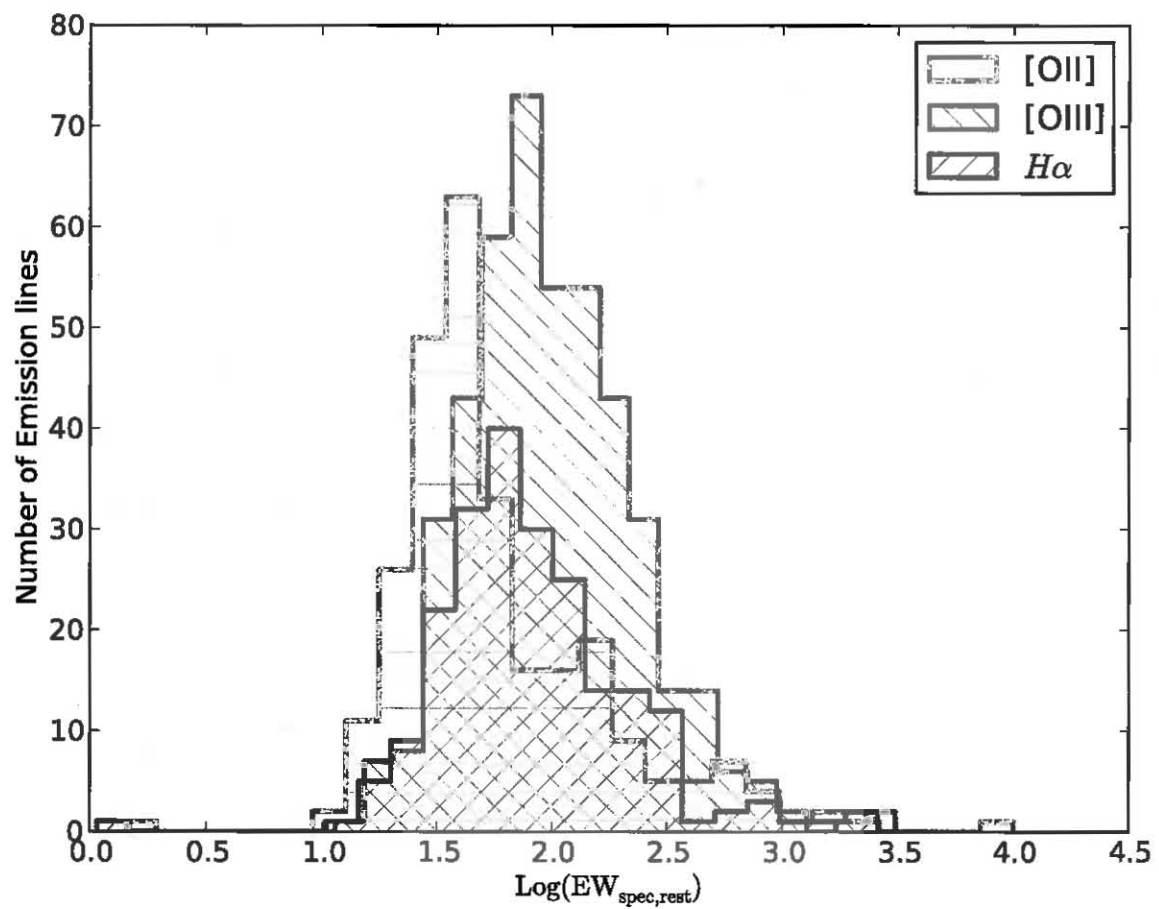


Fig. 3.— Rest-frame spectroscopic EW in the PEARS sample. The median EW_{spec} we measure are 43\AA , 89\AA , and 69\AA for [OII], [OIII], $H\alpha$ emission lines, respectively.

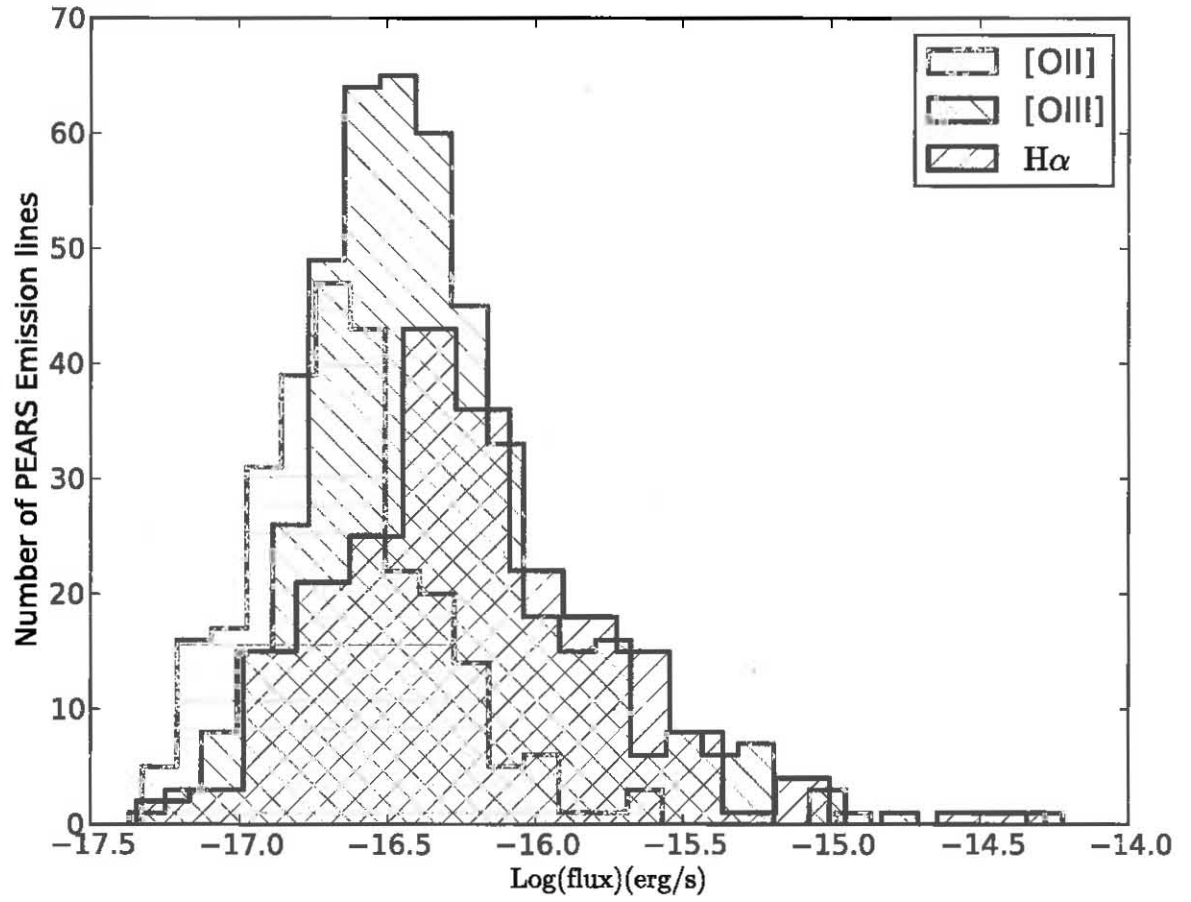


Fig. 4.— Distributions of observed line fluxes in the PEARS sample, uncorrected for completeness or extinction.

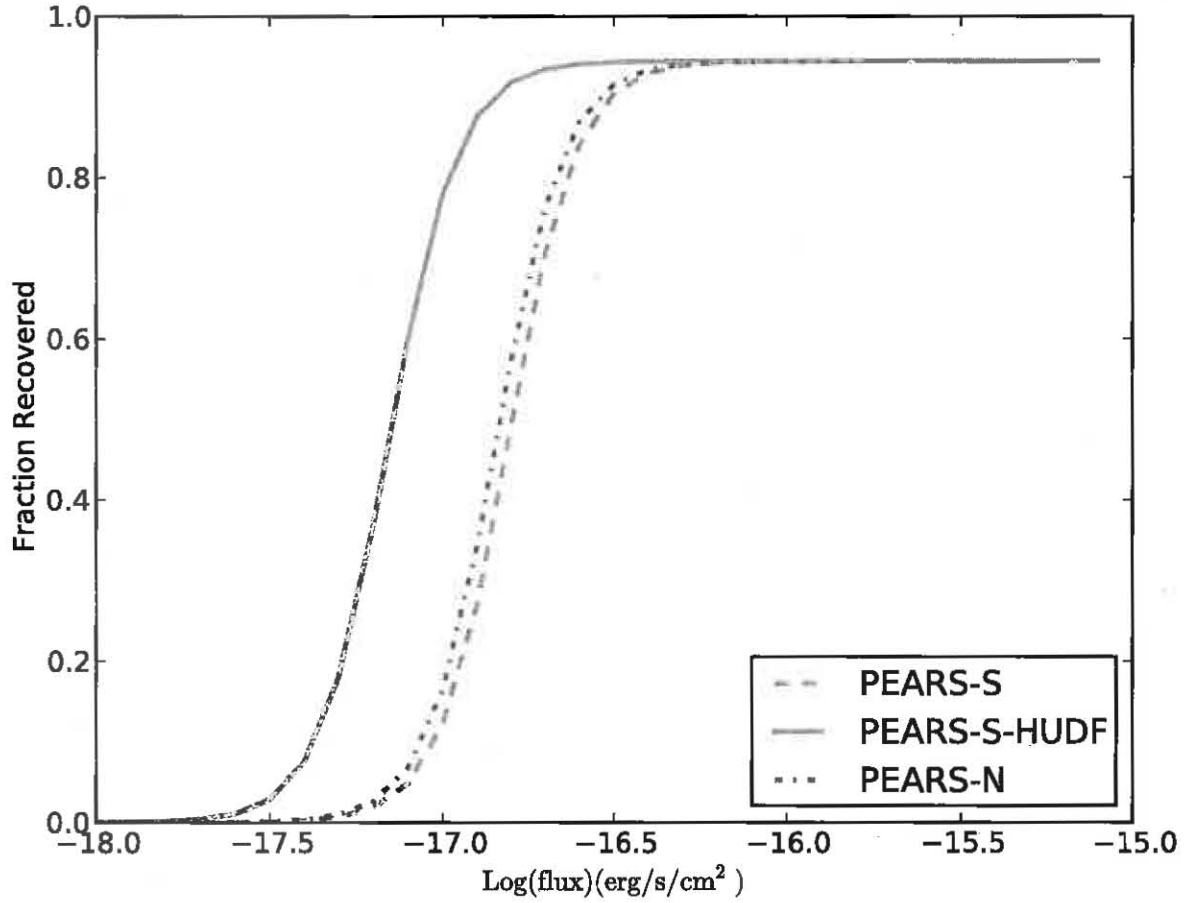


Fig. 5.— PEARS sensitivity to emission line flux. Based on our simulations, we estimate that we can reliably detect emission lines with fluxes greater than $3 \times 10^{-17} \text{ erg/s/cm}^2$ over the whole PEARS fields while the PEARS-S-HUDF field, which was observed twice as long as each of the other 8 fields, reaches line fluxes approximately 1.4 times fainter.

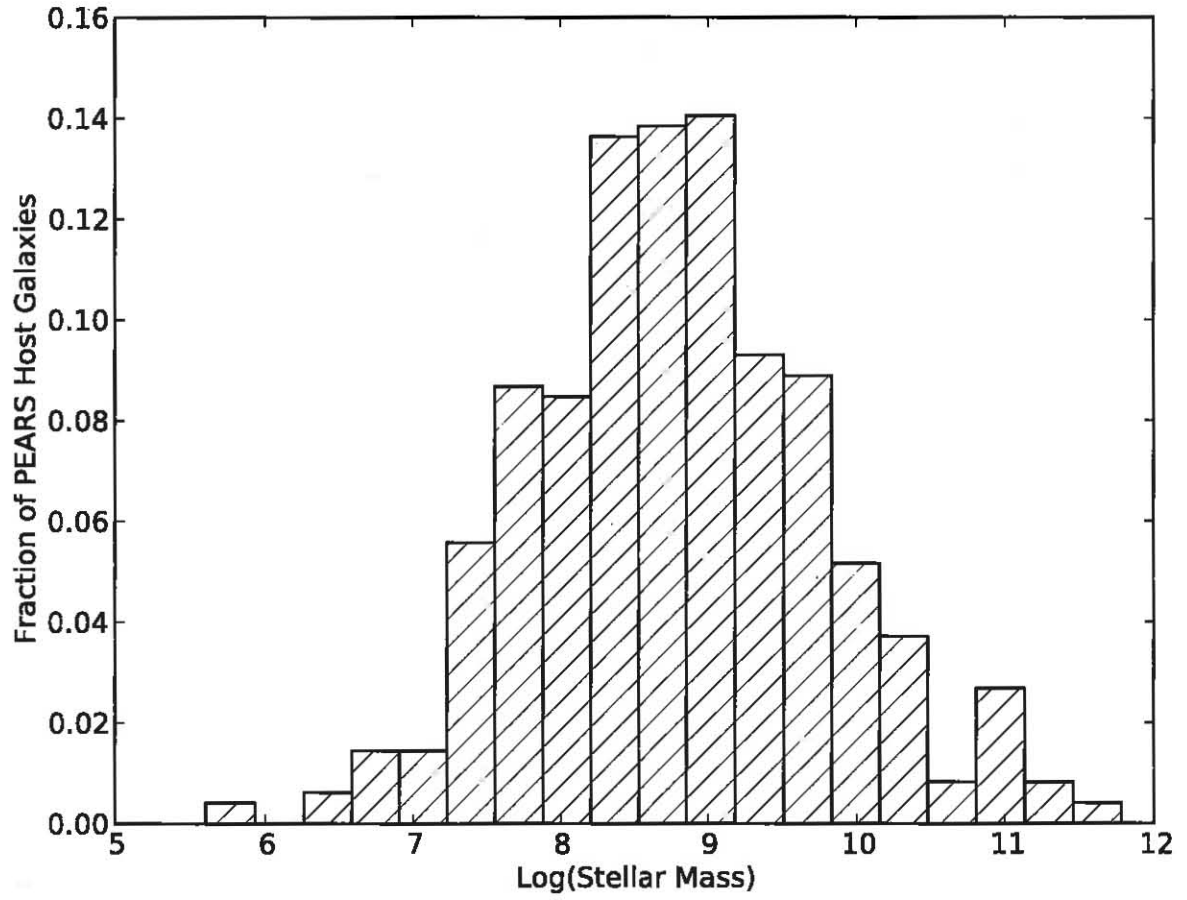


Fig. 6.— Histogram of the PEARs emission line galaxies stellar masses as determined from SED fitting.

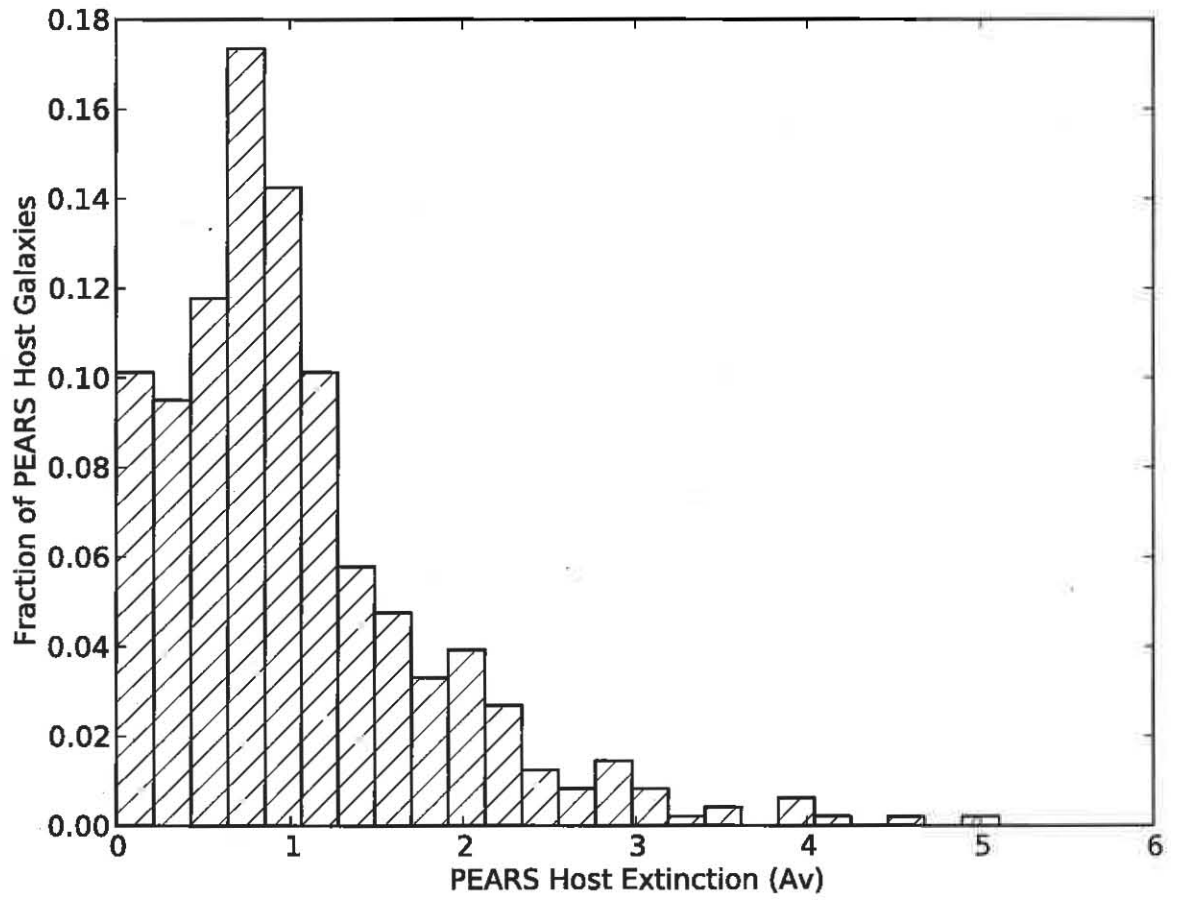


Fig. 7.— Histogram of the PEARs emission line galaxies extinction (A_V) as determined from SED fitting.

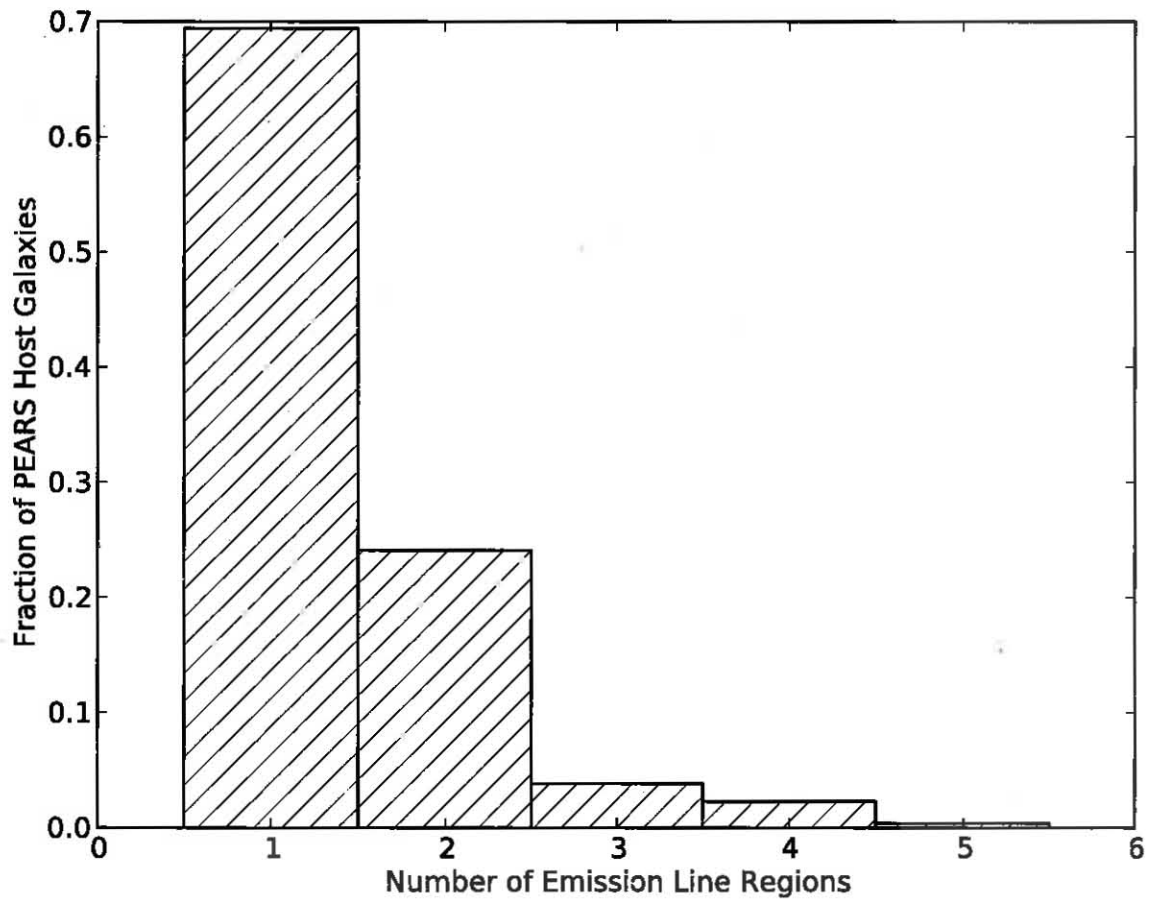


Fig. 8.— Distribution of the number of PEARs emission line regions).

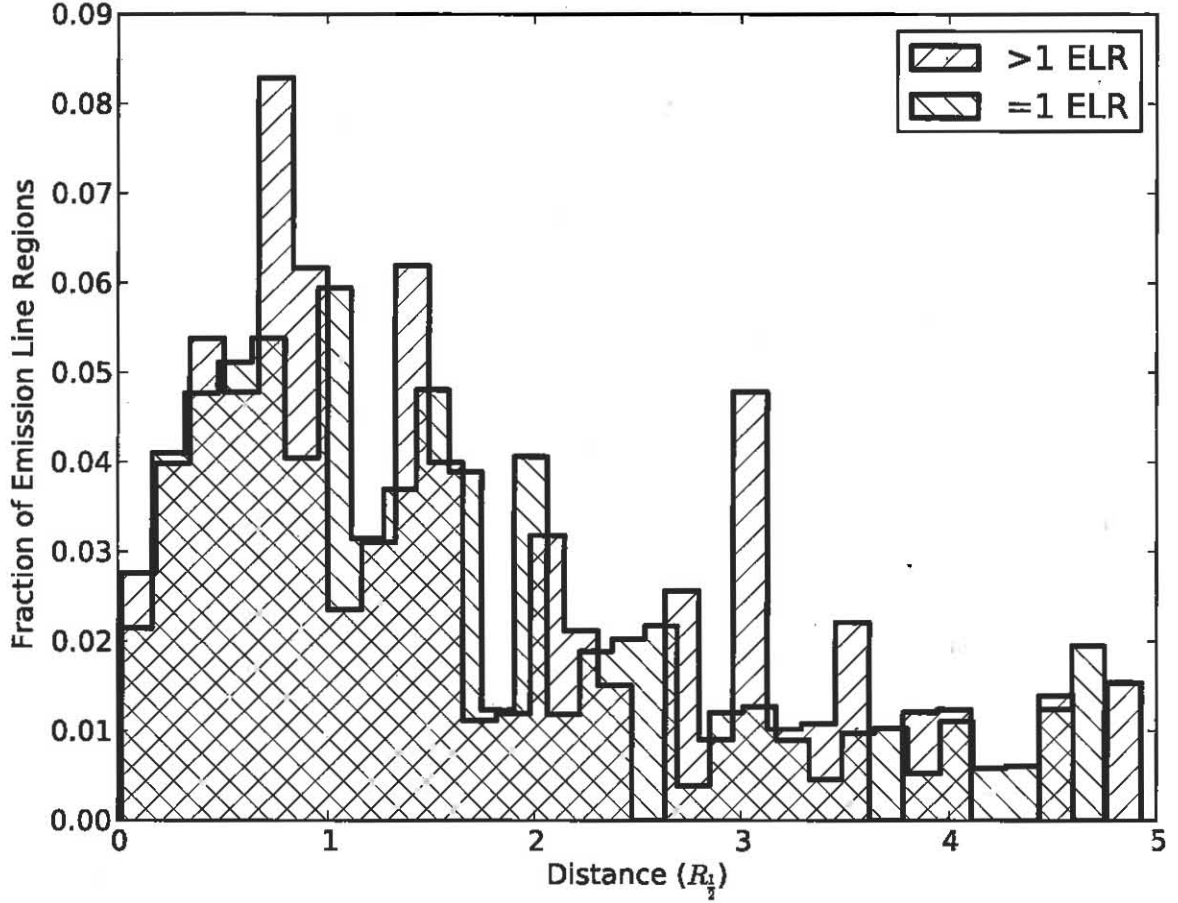


Fig. 9.— Histogram of the distance of the PEARS ELRs from the center of their host galaxies. We show the distribution of ELRs in ELGs where only one ELR was identified as well as the distribution of ELRs in ELGs where more than one ELR was identified. There is no evidence that these distributions are different and a K-S test p-value of 0.49 confirms this.

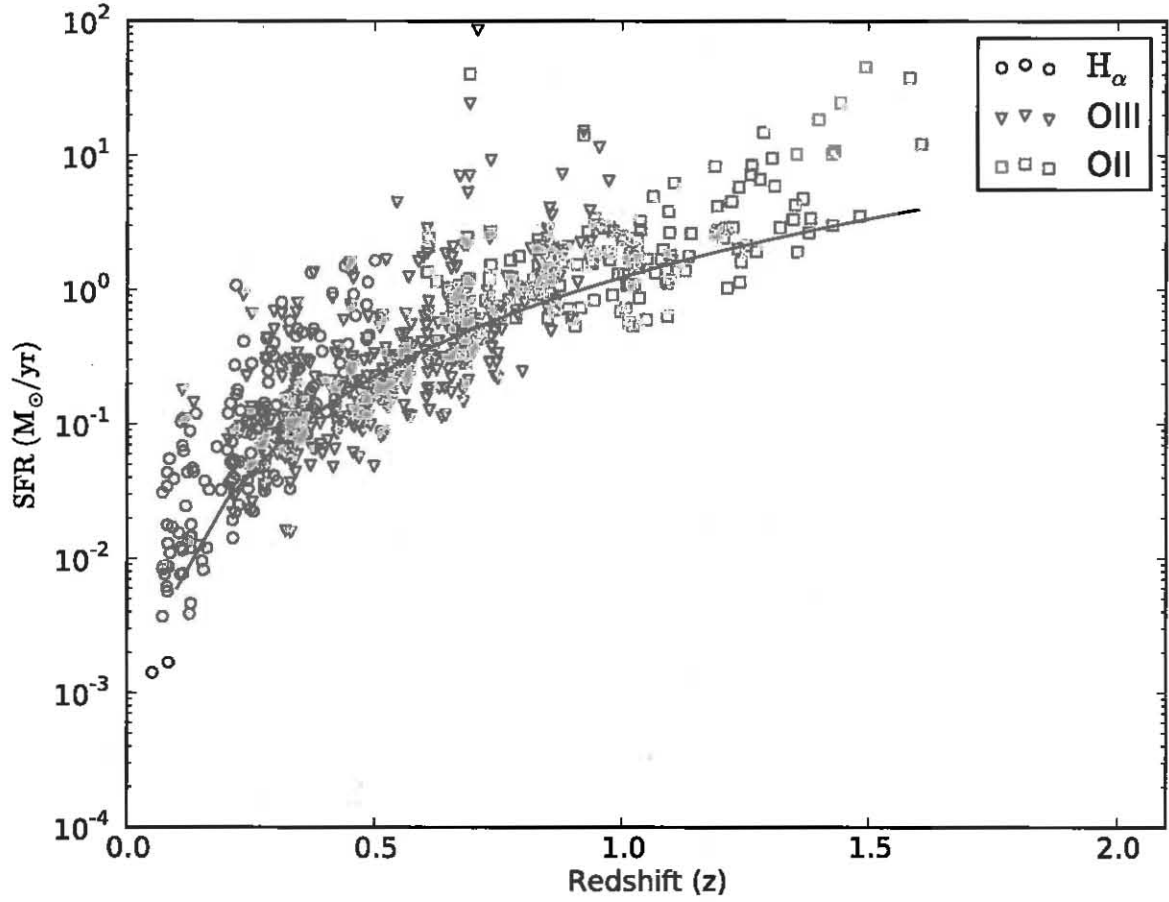


Fig. 10.— Star formation rate as a function of redshift for the PEARs [OII] [OIII] and H_{α} sources with a line grade greater than 2.5. The solid black line shows the star formation rate corresponding to a flux limit of 3×10^{-17} erg/s.

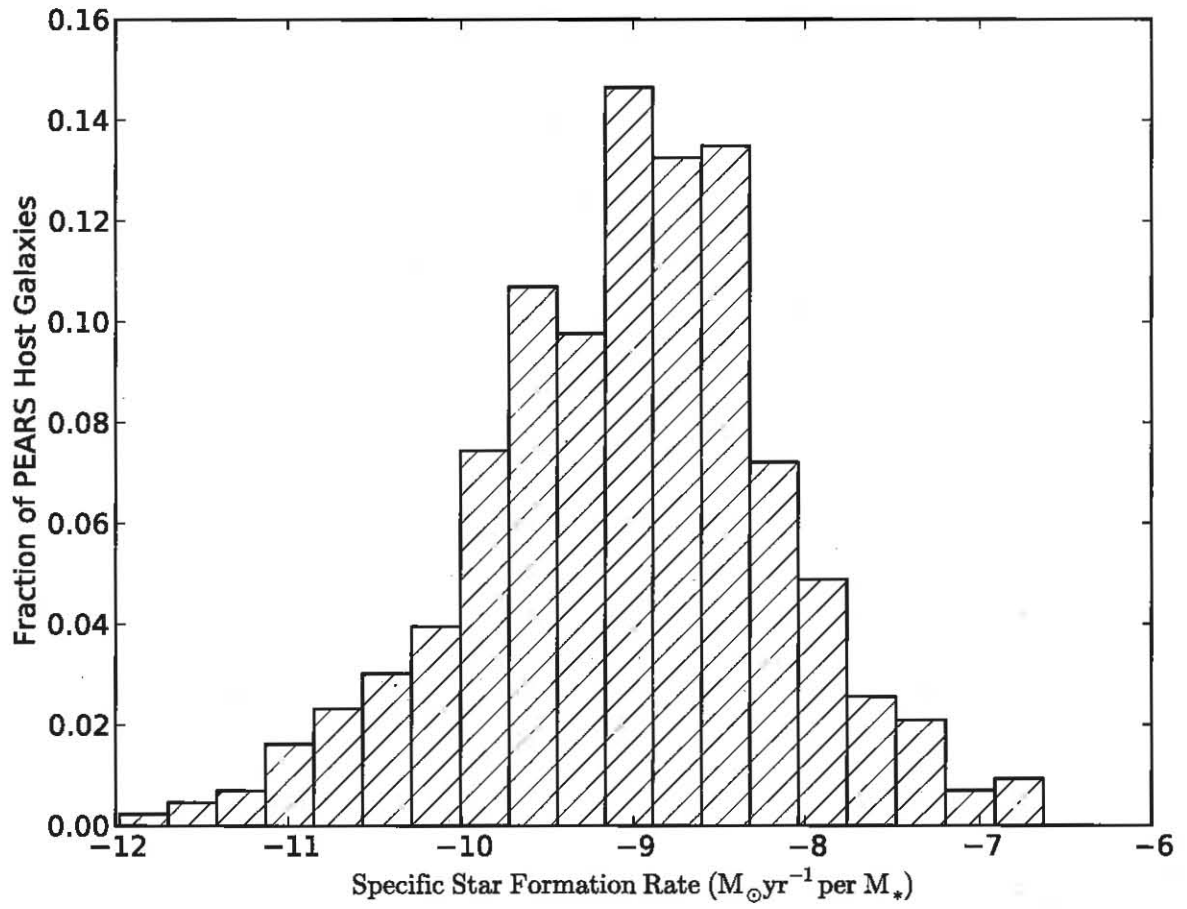


Fig. 11.— Distribution of specific star formation rates for the PEARs host galaxies.).

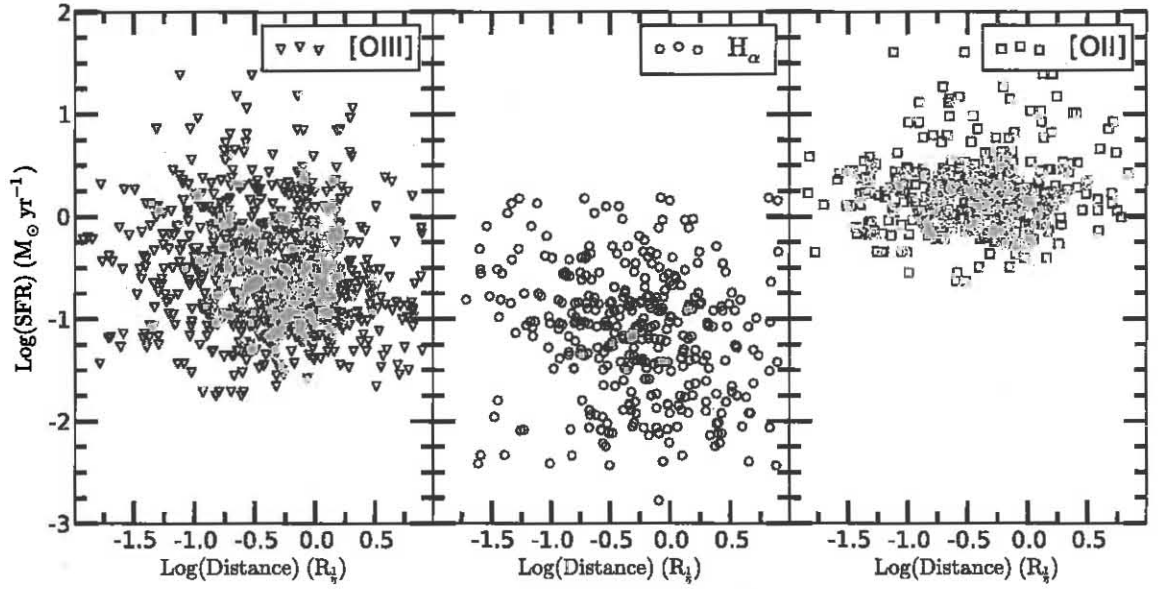


Fig. 12.— Star formation rates of the PEARS emission line regions plotted as a function of their radial position in their host galaxy, normalized to the half light radius of the host galaxy). The amount of star formation appears nearly completely uncorrelated to the location of the LER in the host galaxy with Pearsons correlation coefficients of -0.05, -0.001 and 0.04 for [OIII], H $_{\alpha}$ and [OII], respectively.

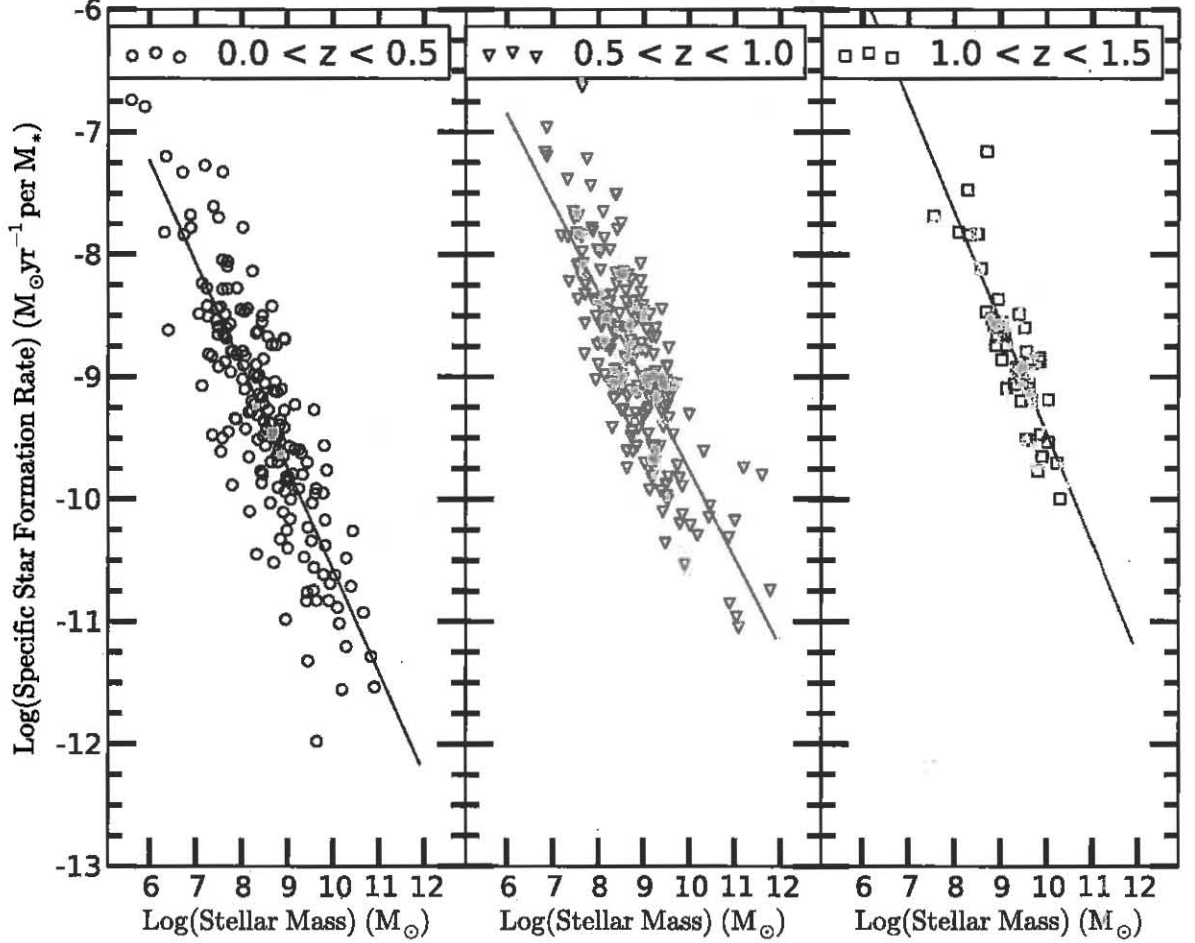


Fig. 13.— Specific star formation rates as a function of host galaxy stellar masses for the PEARS sample. We show three redshift ranges ($0 < z < 0.5$, $0.5 < z < 1.0$ and $1.0 < z < 1.5$, left to right panel, respectively), corresponding to the approximate redshift ranges of $\text{H}\alpha$, $[\text{OIII}]$ and $[\text{OII}]$ in the PEARS grim survey. The relation between sSFR and host galaxy stellar mass are nearly linear with slopes of -0.83 ± 0.04 , -0.73 ± 0.04 and -0.91 ± 0.09 and are statistically identical. The Pearsons correlation coefficient of these fits are -0.84, -0.80 and -0.90, respectively, indicative of a very strong linear correlation.

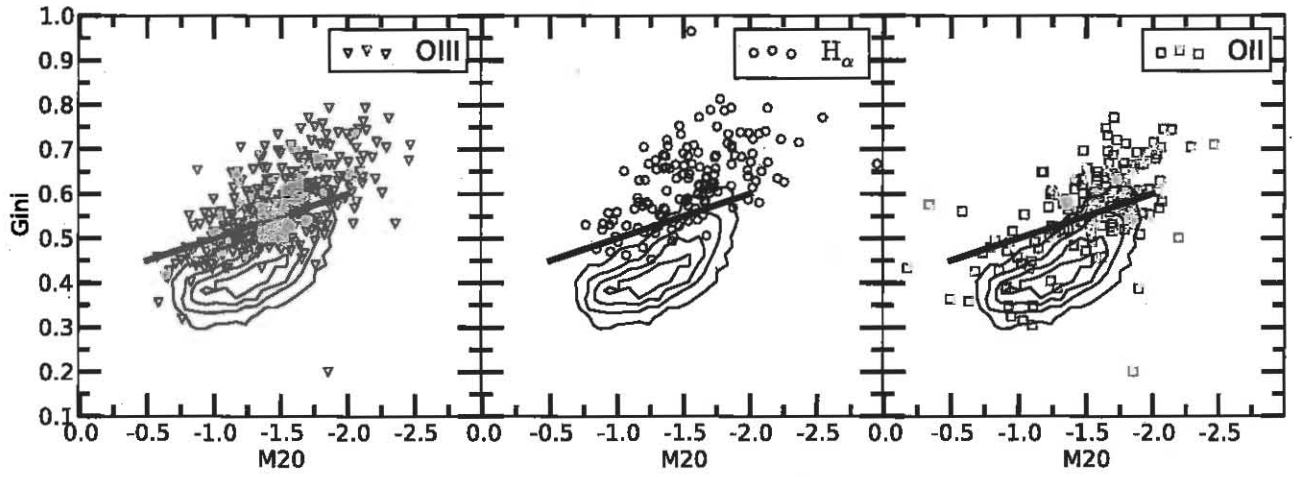


Fig. 14.— Morphology of the PEARs emission line knot host galaxies as parametrized by the Gini and M20 coefficients at the rest-frame wavelength of 4350\AA . This figure shows the rest-frame morphologies of the GOODS field objects (black contours) as well as the host galaxies of our [OII], [OIII], and $H\alpha$ PEARs emission knots (red square, green triangle and blue circle, respectively). The hosts of the emission lines we detected are nearly all above the line (shown in black) separating "normal" galaxies (below the line) and star forming ULIRGs in the nearby Universe (Lotz 2004).

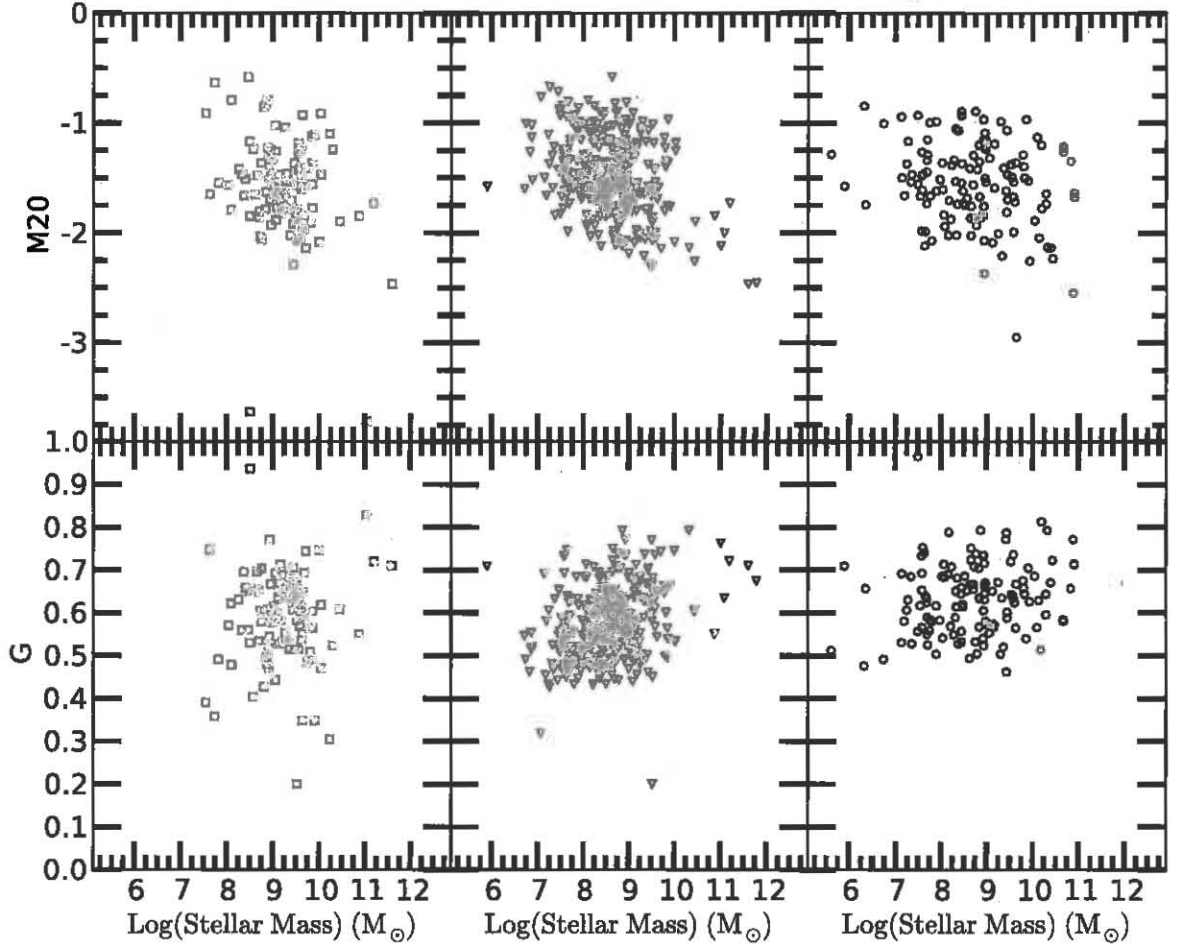


Fig. 15.— Gini coefficient values of the PEARs host galaxies versus their stellar masses, as estimated from SED fitting. The M20 and the Gini values are shown in the top and bottom row, respectively. We also show the [OII], [OIII] and H α host galaxies separately in the left, middle and right most column respectively. There is little evidence for a strong trend between stellar mass and either the M20 or Gini coefficients in our PEARs emission line host galaxies, as indicated by Pearson's correlation coefficient values of at most ≈ 0.16 . However, a mild decrease in M20 and increase in the Gini coefficient as stellar mass increases can be seen for the [OIII] and H α host galaxies (at redshifts of $0.1 < z < 0.9$ and $0 < z < 0.5$ respectively).

REFERENCES

- Bertin, E., & Arnouts, S. 1996, *A&AS*, 117, 393
- Cardelli, J. A., Clayton, G. C., & Mathis, J. S. 1989, *ApJ*, 345, 245
- Cowie, L. L., Songaila, A., Hu, E. M., & Cohen, J. G. 1996, *AJ*, 112, 839
- Dahlen, T., Mobasher, B., Dickinson, M., et al. 2010, *ApJ*, 724, 425
- Dahlen, T. et al., in prep.
- Drozdovsky, I., Yan, L., Chen, H.-W., et al. 2005, *AJ*, 130, 1324
- Efstathiou, G., Ellis, R. S., Peterson, B. A., 1988, *MNRAS*, 232
- Freedman, David; Diaconis, P. (1981). "On the histogram as a density estimator: L2 theory", *Zeitschrift fr Wahrscheinlichkeitstheorie und verwandte Gebiete* 57 (4): 453476.
- Grogin, N. A et al., in prep.
- Guo, Y., Giavalisco, M., Ferguson, H. C., Cassata, P., & Koekemoer, A. M. 2011, *arXiv:1110.3800*
- Hopkins, A. M., Connolly, A. J., Haarsma, D. B., & Cram, L. E. 2001, *AJ*, 122, 288
- Hopkins, A. M. 2004, *ApJ*, 615, 209
- Juneau, S., Dickinson, M., Alexander, D. M., & Salim, S. 2011, *ApJ*, 736, 104
- Kennicutt, R. C., Jr. 1998, *ARA&A*, 36, 189
- Koekemoer, A. M., Fruchter, A. S., Hook, R. N., & Hack, W. 2002, in *Proc. 2002 HST Calibration Workshop*, ed. S. Arribas, A. Koekemoer, & B. Whitmore (Baltimore: STScI), 33
- Laidler, V. G., Papovich, C., Grogin, N. A., et al. 2007, *PASP*, 119, 1325
- Lotz, J. M., Primack, J., & Madau, P. 2004, *AJ*, 128, 163
- Lotz, J. M., Jonsson, P., Cox, T. J., & Primack, J. R. 2008, *MNRAS*, 391, 1137
- Lotz, J. M., Jonsson, P., Cox, T. J., & Primack, J. R. 2010, *MNRAS*, 404, 590
- Ly, C., et al. 2007, *ApJ*, 657, 738

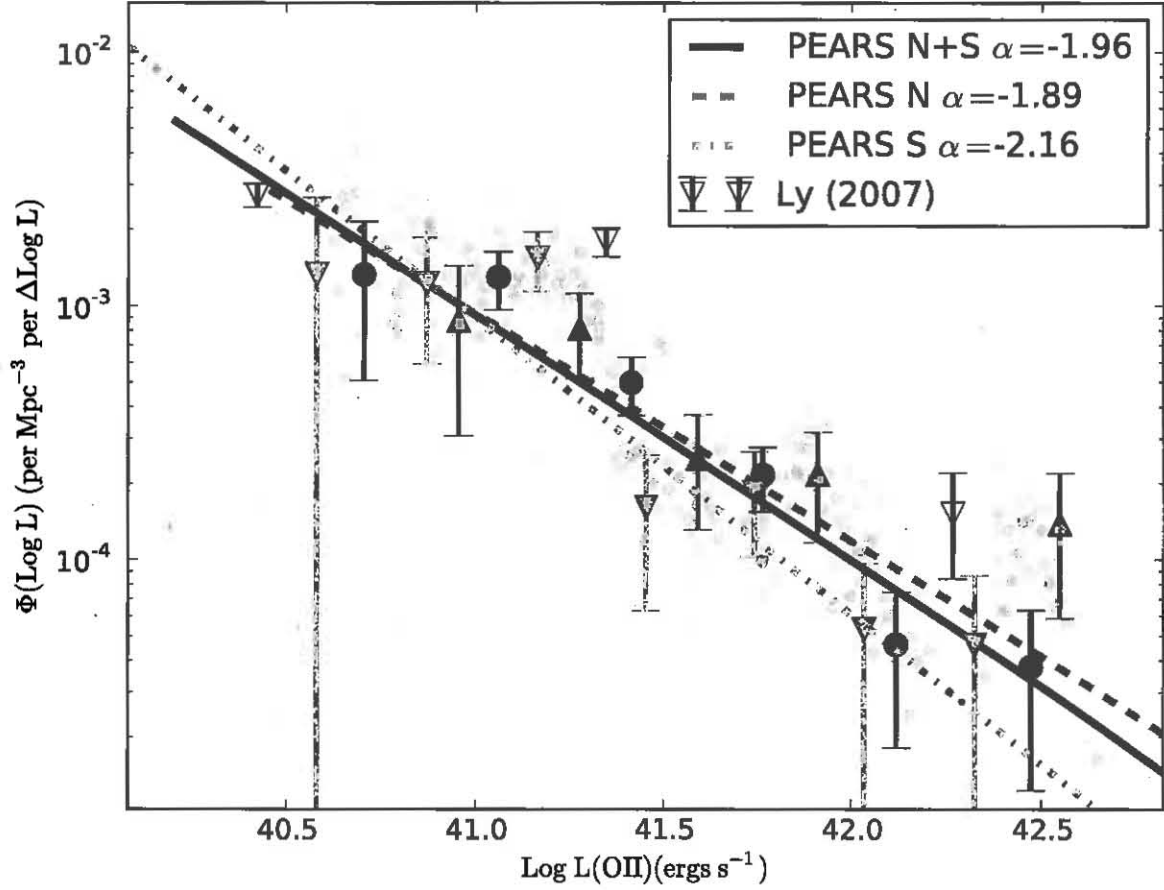


Fig. 16.— PEARS [OII] luminosity function. We show the full PEARS, PEARS-N and PEARS-S in black, blue, and red, respectively. The solid circles with error-bars show the $1/V_{\max}$ results while the solid lines are fits to the $1/V_{\max}$ results. We see no significant differences between the PEARS-N and PEARS-S fields. We also plot the sample of [OII] emitters from Ly et al. (2007), also with no dust correction and excluding objects with $EW < 50\text{\AA}$ from their sample so that we can better compare our results.

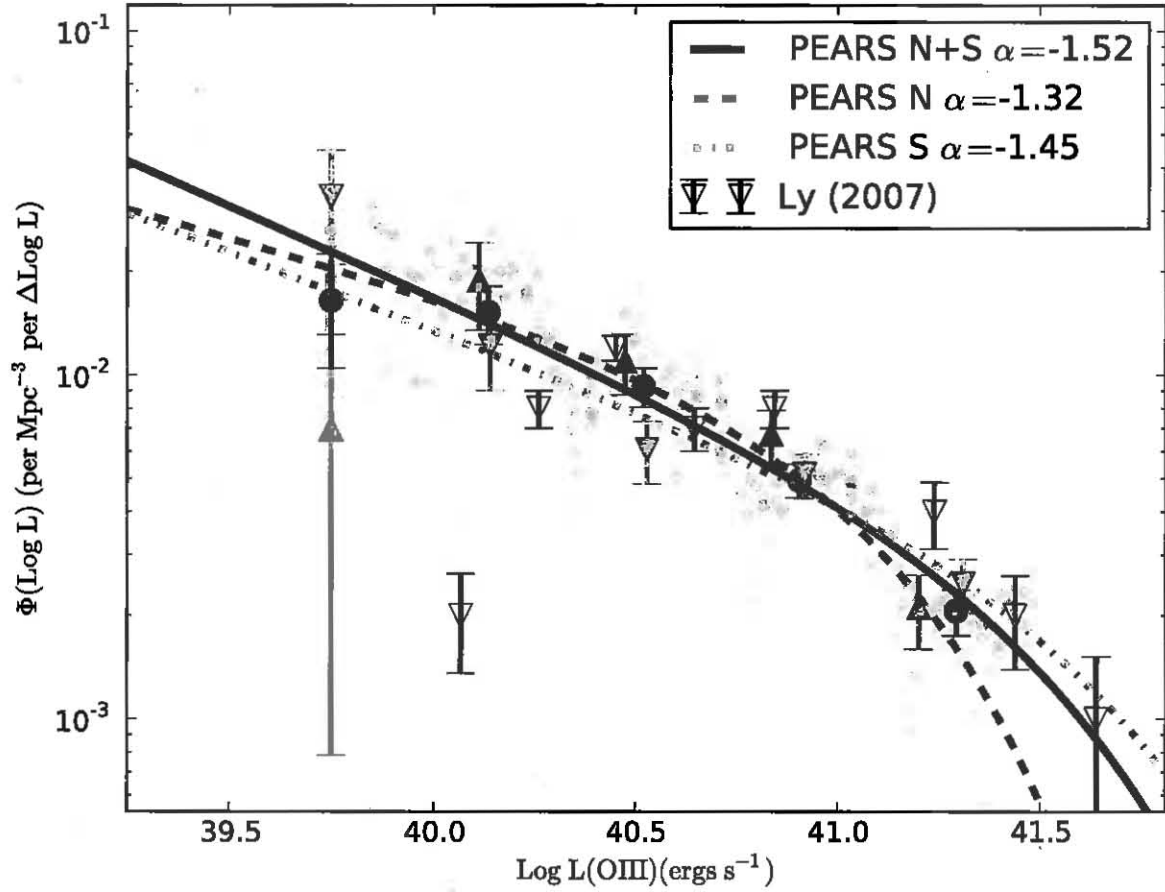


Fig. 17.— PEARS [OIII] luminosity function. We now show the full PEARS, PEARS-N and PEARS-S in black, blue, and red, respectively. The solid circles with error-bars show the $1/V_{\text{max}}$ results while the solid lines are fits to the $1/V_{\text{max}}$ results. We see no significant differences between the PEARS-N and PEARS-S fields. We also plot the sample of [OII] emitters from Ly et al. (2007), also with no dust correction and excluding objects with $\text{EW} < 50\text{\AA}$ from their sample so that we can better compare our results.

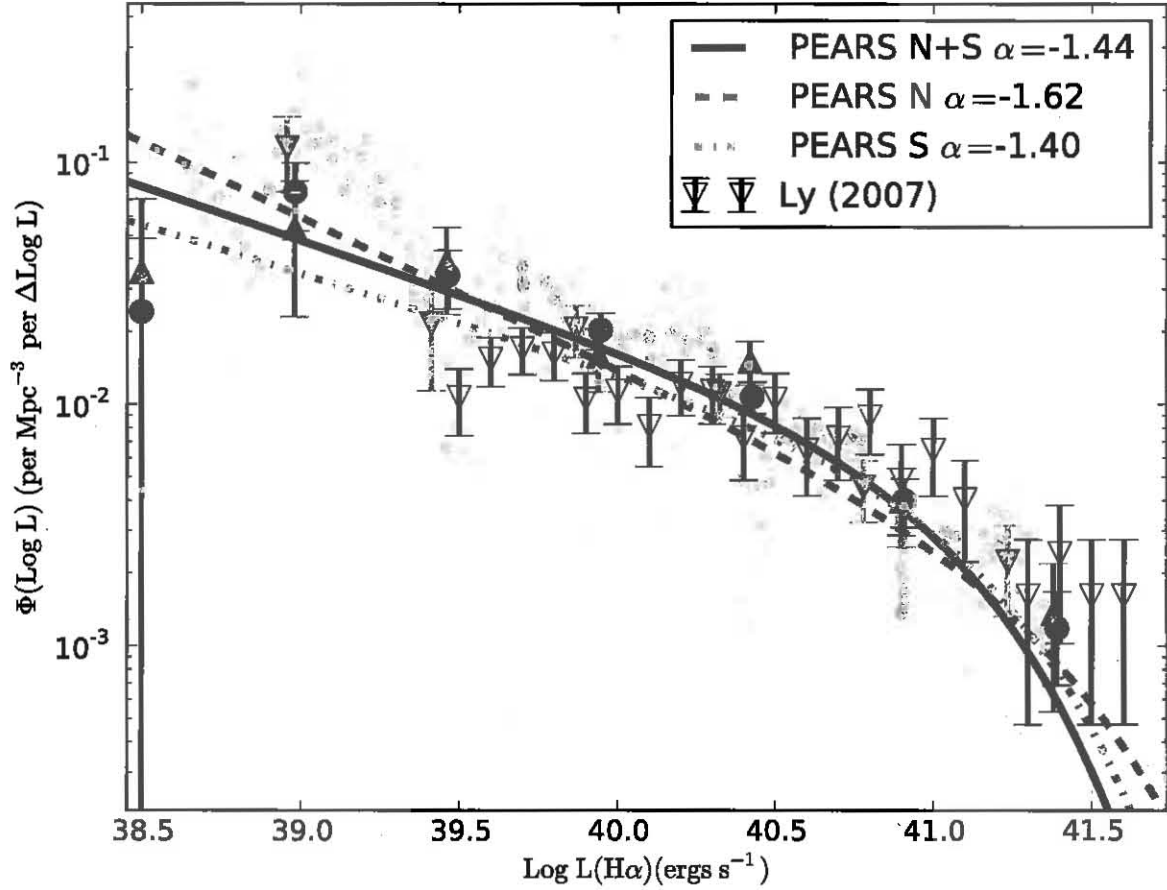


Fig. 18.— PEARS $H\alpha$ luminosity function. We now show the full PEARS, PEARS-N and PEARS-S in black, blue, and red, respectively. The solid circles with error-bars show the $1/V_{\max}$ results while the solid lines are fits to the $1/V_{\max}$ results. We see no significant differences between the PEARS-N and PEARS-S fields. We also plot the sample of [OII] emitters from Ly et al. (2007), also with no dust correction and excluding objects with $EW < 50\text{\AA}$ from their sample so that we can better compare our results.

- Madau, P., Pozzetti, L., & Dickinson, M. 1998, *ApJ*, 498, 106
- Pirzkal, N., Pasquali, A., & Demleitner, M. 2001, *ST-ECF Newslett.*, 29, 5
- Noeske, K. G., Faber, S. M., Weiner, B. J., et al. 2007, *ApJ*, 660, L47
- Pirzkal, N., Xu, C., Malhotra, S., et al. 2004, *ApJS*, 154, 501
- Pirzkal, N., Xu, C., Ferreras, I., et al. 2006, *ApJ*, 636, 582
- Pirzkal, N., Burgasser, A. J., Malhotra, S., et al. 2009, *ApJ*, 695, 1591
- Pirzkal, N., Rothberg, B., Nilsson, K. K., et al. 2012, *ApJ*, 748, 122
- Sandage, A., Tammann, G. A., & Yahil, A. 1979, *ApJ*, 232, 352
- Schechter, P. 1976, *ApJ*, 203, 297
- Straughn, A. N., Meurer, G. R., Pirzkal, N., et al. 2008, *AJ*, 135, 1624
- Straughn, A. N., Pirzkal, N., Meurer, G. R., et al. 2009, *AJ*, 138, 1022
- Takahashi, M. I., Shioya, Y., Taniguchi, Y., et al. 2007, *ApJS*, 172, 456

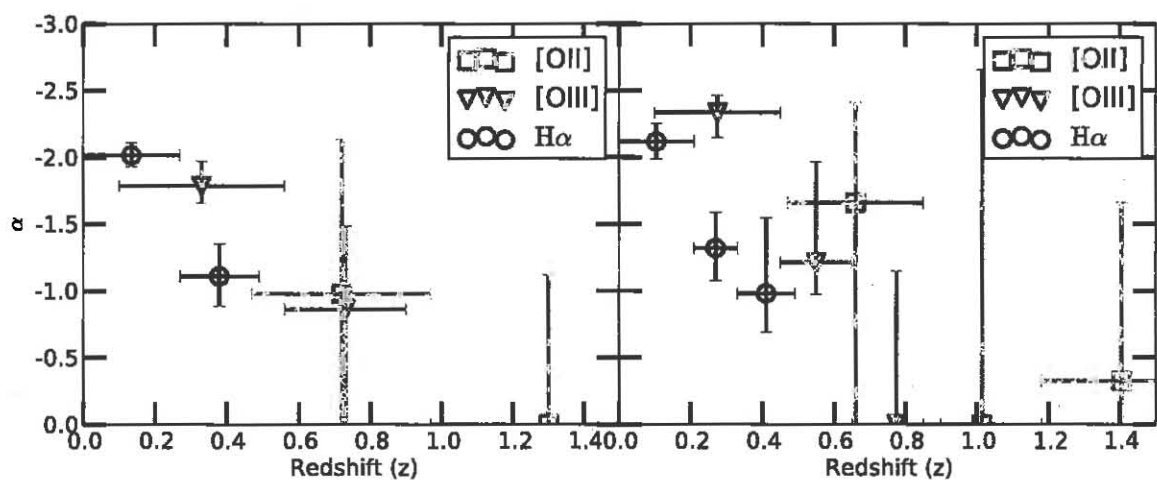


Fig. 19.— Slope of the PEARs [OII], [OIII], and H α luminosity functions as a function of redshift when considering two separate redshift ranges (left panel) or three separate redshift ranges (right panel). A clear trend is seen when splitting our samples in halves whereby the slope of the luminosity function is measured to flatten as redshift increases. This trend is still present, albeit with now more noisy estimates of the luminosity slopes, when splitting out sample in three.

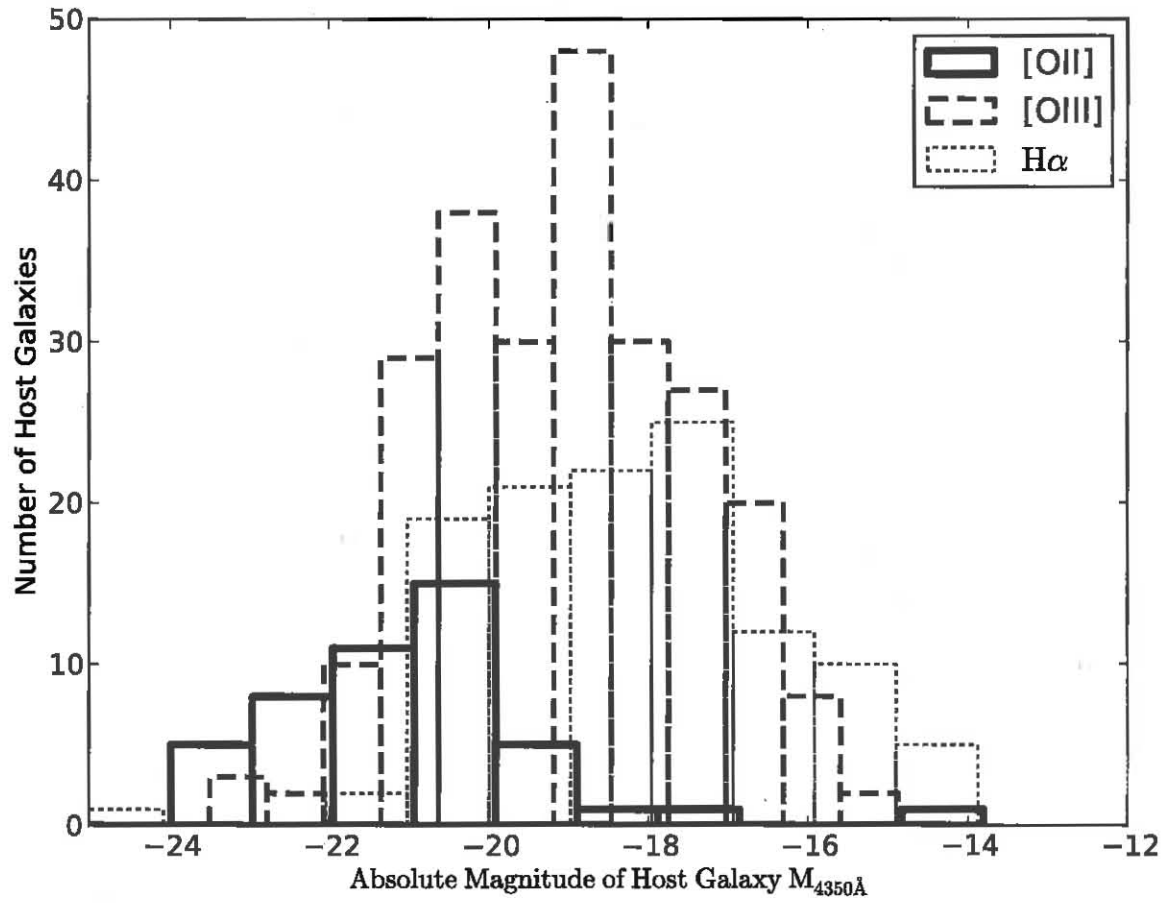


Fig. 20.— Distributions of the 4350\AA rest-frame absolute magnitude of the host galaxies of the PEARS [OII] [OIII] and $H\alpha$ emission line.

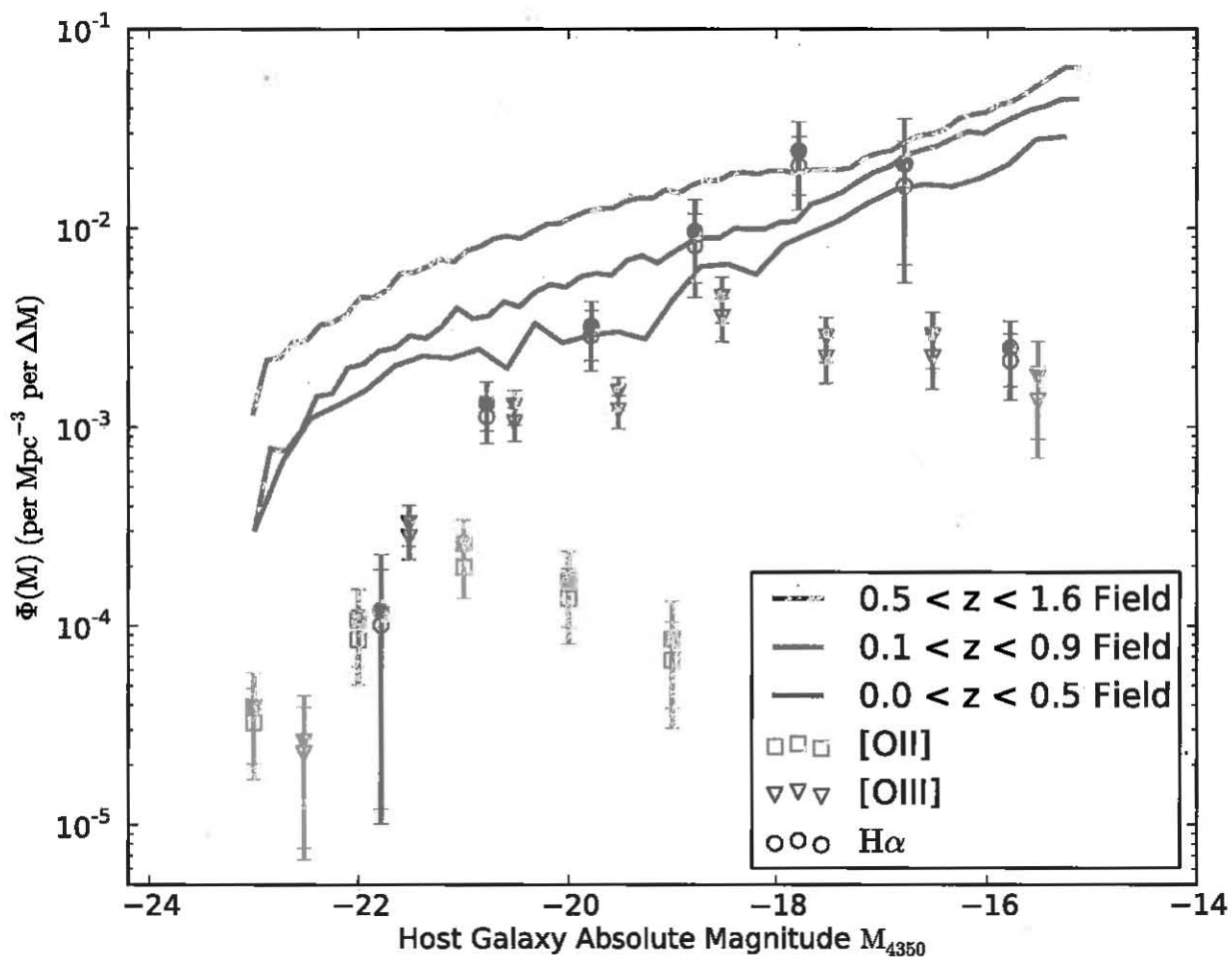


Fig. 21.— Luminosity functions of the 4350\AA rest-frame absolute magnitude of the host galaxies of the PEARS [OII] [OIII] and $H\alpha$ emission line (symbols with error bars). The luminosity function of GOODS field galaxies are shown (scaled) using solid lines. The density of $H\alpha$ emitters ($0 < z < 0.5$) peaks at ≈ -18 , while the density of [OIII] emitters peaks at ≈ -19 and the density of [OII] emitting galaxies ($0.5 < z < 1.6$) peaks at ≈ -21 . We show both the completeness corrected (filled symbols) and uncorrected (open symbols) density estimates.